Analysis of Passive Magnetic Inspection Signals Using the Haar Wavelet and Asymmetric Gaussian Chirplet Model (AGCM)

by

Roozbeh Rahimijurabi

A thesis

presented to the University of Waterloo

in fulfillment of the

thesis requirement for the degree of

Master of Applied Science

in

Civil Engineering

Waterloo, Ontario, Canada, 2022

Author’s Declaration

I hereby declare that I am the sole author of this thesis. This is a true copy of the thesis, including any required final revisions, as accepted by my examiners.

I understand that my thesis may be made electronically available to the public.

Abstract

Nowadays, Non-Destructive Testing (NDT) techniques are an essential foundation of infrastructure retrofit and rehabilitation plans, mainly due to the huge amount of construction, as well as the high cost of demolition and reconstruction. Modern NDT methods are moving toward automated detection methods to increase the speed and probability of detection, which enlarges the size of inspection data and raises the demand for new data analysis methods.

NDT methods are divided into two main groups; active and passive. The external potentials are discharged into an object in an active method, and then the reflection wave is recorded. However, the passive methods use the self-created magnetic field of the object. Therefore, the magnetic value of ferromagnetic material in a passive method is less than the magnetic value of an active method, and defects and anomalies detection needs more variety of functional signal processing methods. The Passive Magnetic Inspection (PMI) method, as an NDT-passive technology, is used in this thesis for ferromagnetic materials quantitative assessment. The success of the PMI depends on the detection of anomalies of the passive magnetic signals, which is different for every single test. This research aims to develop appropriate signal processing methods to enhance the PMI quality of defect detection in ferromagnetic materials.

This thesis has two main parts and presents two computer-based inspection data analysis methods based on the Haar wavelet and the Asymmetric Gaussian Chriplet Model (AGCM). The Passive Magnetic Inspection method (PMI) is used to scan ferromagnetic materials and produce the raw magnetic data analyzed by the Haar wavelet and AGCM.

The first part of this study describes the Haar wavelet method for rebar defect detection. The Haar wavelet is used to analyze the PMI magnetic data of the embedded reinforcement steel rebar. The

corrugated surface of reinforcing steel makes the detection of defects harder than in flat plates. The up and down shape of the Haar wavelet function can filter the repeating corrugations effect of steel rebars on the PMI signal and thereby better identify the defects. Toogood Pond Dam piers' rebar defects, as a case study, were detected using the Haar wavelet analysis and verified by the Absolute Gradient (AG) method using visual comparison of the resultant signals and the correlation coefficient. The predicted number of points with a rebar area loss higher than 4% is generally the same with the AG and the Haar wavelet methods. The mean correlation coefficient between the signals analyzed using the AG and the Haar wavelet for all rebars is 0.8.

In the second part of this study the use of the AGCM to simulate PMI signals is investigated. Three rail samples were scanned to extract a three-dimensional magnetic field along specific PMI transit lines of each sample for the AGCM simulations. Errors, defined as the absolute value of the difference between signal and simulation, were considered as a measure of simulation accuracy in each direction. The samples' lengths differed, therefore error values were normalized with respect to the length to scale data for the three samples. The Simulation Error Factor (SEF) was used to measure the error and sample 3 showed the lower value. Finally, statistical properties of the samples' SEF, such as standard deviation and covariance, were evaluated, and the best distribution was fitted to each of the data sets based on the Probability Paper Plot (PPP) method. The Log-Normal probability distribution demonstrated the best compatibility with SEF values. These distributions and statistical properties help to detect outlier data for future data sets and to identify defects.

Acknowledgements

I want to show my deepest appreciation to my supervisor Prof. Maurice Dusseault who supported me from the first day of application for the master of science program at the University of Waterloo and during my education and allowed me to pursue my dreams to graduate from a top-ranked University in Canada.

I will never forget the kind support of Prof. Cascante, my co-supervisor, who helped me on challenging path of my MSc, and treated me as his friend. Prof. Cascante showed me how valuable it is to assist people when they need us.

I want to express my deepest gratitude to Prof. Wei-Chau Xie for all his kindly support and helping me as the second examiner.

I would like to warmly thank Prof. Potapenko, who read my thesis as the third examiner and kindly provided me with his valuable ideas.

SeyedBijan Mahbaz is the person who changed my way of life forever. From the first day of my education, his patience to answer my academic questions and his strong scientific background helped me follow my program much better. Besides great academic support, he treated me as his family, and that's why I enjoyed every moment of working with him.

I would like to thanks Prof. Hassan Baaj for giving me a new perspective of academic papers and Prof. Mahesh Pandy for his helpful Risk and Reliability knowledge.

I would like to express my appreciation to InspecTerra Inc. for providing access to the PMI device used in this study. I would also like to thank the City of Markham for providing access to Toogood Dam site and related documents.

Finally, I want to thank my wife Rezvan Barzegar who was my biggest supporter during my studies.

Dedication

To my loving wife Rezvan,
And to my wonderful parents

Table of Contents

List of Figures

List of Tables

List of Nomenclatures

A_j = wavelet approximation signal.

$A_p(t)$ = asymmetric Gaussian chirplet function.

a_m = weighting factor for the mth selected atom.

B = magnetic flux density.

C = positive constant with a predetermined value.

D_j = wavelet detail signal.

d_m = mth selected atom from the dictionary matrix columns.

E_d = energy of stray magnetic field.

$E_p(t)$ = asymmetric Gaussian chirplet function envelope part.

$F_p(t)$ = asymmetric Gaussian chirplet function frequency part.

$F(x)$ = CDF of the Log-Normal distribution.

f = center frequency.

H = external magnetic field.

H_d = stray magnetic field.

$h_i(x)$ = Haar wavelet function.

$\boldsymbol{J_s}$ = magnetization saturation.

j = dilation index or scale factor.

J = magnetic polarization.

k = translation index or shift factor.

M = magnetization.

n = normal vector at the separation surface of the two materials.

$R_j(t)$ = residual value.

r = vector of position.

V = the volume of the element.

y = real signal.

$\hat{y}$ = approximated signal.

α = bandwidth factor.

β = asymmetry factor.

γ = chirp rate.

λv = volume charge density.

θ = phase angle.

μ_0 = vacuum magnetic permeability.

$\phi_{j,k}$ = wavelet scaling function.

$\psi_{j,k}$ = wavelet function.

τ = time shift factor.

PART ONE

The Haar Wavelet Decomposition Method for Concrete Reinforcement Assessment

Chapter 1

Literature Review

Using signal processing methods to detect various types of defects or anomalies has been discussed extensively by researchers over the last two decades. The Wavelet Transform (WT) approach with different basic wavelet forms such as Symlet, Haar, etc., comprises one of the signal processing methods with a wide range of application.

Saadatmorad *et al.* (2021) used the wavelet transform (WT) with a Neural Network to detect damage in Rectangular Laminated Composite Plates (RLCPs). In this approach, the location of the defects was detected using a two-dimensional wavelet and convolutional neural networks. An FEM model of damaged elements was developed to gather two-dimensional wavelet feed signals. They stated that the proposed method was able to detect defects in RLCPs with high accuracy.

Elefante et al. (2019) gathered photodiode signals by monitoring laser-welded butt joints and analyzed them with a continuous wavelet transform. In this method, the laser-welded butt joints are assessed by a photodiode system that evaluates the offset between the laser beam and the joint.

Abdulkareem *et al.* (2019) worked on defect detection in steel plates using wavelet transform approaches. The main technical part of their research was eliminating edge distortion problems using a two-dimensional continuous wavelet transform. The mode shape signal of undamaged plates was subtracted from the damaged plate mode shape signal, and the resulted differential signal was decomposed using wavelet transform methods. The results showed that the edge distortion problem was resolved using this proposed method.

A new method to detect delamination in composites using wavelet transform methods was presented by *Feng et al.* (2018). They worked on CFRP (Carbon-Fibre-Reinforced Polymer) plates delamination length assessment and stated that the lowest frequency of the delamination-impacted signal increases when the length of the delamination increases; thereby, delamination length could be estimated.

Zheng *et al.* (2012) showed the drawbacks of averaging, moving averaging, second-order difference, oblique cumulative curve, and short-time Fourier transform data processing methods in traffic engineering. They assessed different WT capabilities for traffic engineering data processing and proved the capability of WT approaches for assessment of such types of data.

Lilong *et al.* (2012) presented a method based on the "denoising" capability of WT for eliminating noises in gyroscope output signals, and they showed that WT analysis led to higher accuracy in the north-seeking function of the gyroscope.

Logistic regression and WT were used by Agarwal (2016) for detecting vehicle incidents. Because of the binary nature of incidents (the presence or absence), the binary logistics function regression model was used in their study. The results demonstrated that using the regression model together with

wavelet feature extraction effectively detects incidents by the equilibrium between the ratio of the incident detection and the false alarm rate.

Sahoo *et al.* (2017) analyzed the discriminative features of electrocardiogram (ECG) signals with WT. They classified cardiac abnormalities into four categories and stated that the error in this abnormalities detection exercise was less than 0.42%.

Li *et al.* (2012) presented a new wavelet decomposition method, Adaptive Morphological Gradient Lifting Wavelet (AMGLW), for identification and assessment of bearing defects. The simulated and measured vibration signals from bearings were used for comparing the proposed AMGLW with a more "traditional" wavelet transform, and the results revealed that the accuracy for detecting bearing defects in AMGLW was obviously higher than in LW and ALW methods alone.

Detection of alcoholism using EGG (Electrogastrography) signals and wavelet transform analysis was the research subject of an article by Anuragi and Sisodia (2020). They used a wavelet transform and a machine learning framework for categorizing EGG signals in normal and alcoholic clients and concluded that the statistical approach referred to as LS-SVM (Least-Squares Support-Vector Machine) was the best classifier for these kinds of data.

Li *et al.* (2012) proposed a method that detected cracked eggshells using wavelet transform methods. They studied the pulse time signals gathered using a microphone when knocking the egg and showed that the energy parameter value between intact and cracked eggs is different.

Albaqami *et al.* (2021) presented an automated method based on Wavelet Packet Decomposition (WPD) method for EGG signals interpretation and extracting of statistical features. Their proposed classification method accuracy was reported to be 87.68%.

Zhang *et al.* (2014) presented a novel application for using wavelet transform approaches. The continuous wavelet analysis (CWA) was compared with some traditional yellow dust disease detection methods, and the results showed the power of the continuous wavelet analysis method for detecting the disease. (Yellow dust is the term for wind-borne dust generated in north-central China and Mongolia, moving toward the south east - eastern China, Korea, Japan)

Kerut et al. (2017) presented a Morlet continuous wavelet transform (CWT) algorithm for Heart Rate Variability (HRV) analysis. The electrocardiogram and respiratory data were recorded and analyzed with the Morlet CWT and a sharp increase in wavelet frequency band of the sympathetic nervous system and the parasympathetic nervous system was observed.

The wavelet transform was used to detect cracks in beams in a study published recently by *Kumar et al.* (2022). The wavelet transform analysis detected operational deflection shape (ODS) discontinuities as crack sites in the beams. The finite element model was employed for quantifying the displacement values, and their results showed an appropriate level of crack detection accuracy in the beams.

A new concept for wavelet transform application detection was introduced by Bhavsar *et al.* (2020). They worked on 3D online printing quality by analyzing the vibroacoustic signals of the printing area and the differences in these signals for strong (intact) and failed first layer filament deposition. The wavelet categorized the signals' energy into different levels, and a clear difference between the energy levels between poor and acceptable bond formation was observed.

The PMI is two-dimension signal of magnetic flux density against time (location). However, the previous rebar defect detection methods, e.g., Absolute Gradient (AG), do not use time-frequency functions to find the defects in steel rebar. Therefore, that methods cannot detect the frequency of

defects and their location at the same time. This part of this research aims to represent a new time-frequency signal processing method based on wavelet for defect detection in reinforced concrete steel rebar using the PMI magnetic signals.

In summary, WT methods have become widely employed in many domains ranging from defect detection to classification methods applied to health data (diagnostic analysis). In this work, the WL based on the Haar wavelet is used for analysis of passive magnetic data collected over ferromagnetic materials with corrosion and cracks.

Chapter 2

Theoretical Background

The central physical concept of magnetic inspection methods is the ferromagnetic materials' magnetic properties. The magnetic properties of ferromagnetic materials can reflect their structural and mechanical properties and be impacted by alterations in stress, the presence of anomalies (cracks, corrosion), and other factors. Defects like general corrosion, corrosion centers such as pitting, and cracks lead to anomalies. Massive (plastic) strains and high stress levels in ferromagnetic materials can lead to changes in metal crystal structure and alteration of structural properties of these materials; these may be detected by magnetic methods (Blitz, 1997).

Internal inhomogeneity of ferromagnetic materials arising from various sources can be assessed by measuring their inductive magnetic field. The magnetic field of an intact, non-damaged ferromagnetic material under a uniform value of induced magnetization is constant. However, any physical change in the specimen (shape changes, cracks, corrosion, plastic strains, etc.) alters the magnetic response and generates a change in the magnetic flux lines – either from active or passive magnetic fields. This is because of the magnetic leakage that is associated with cracks, pitting, corrosion, or any other types of discontinuities and associated crystal changes (ASME, Vol. 17). Active magnetic methods employing strong external magnetic field application include magnetic flux measurements, magnetic particle inspection, and electromagnetic microwave testing. Passive methods do not use an externally applied magnetic field, but rely on detecting anomalies (distortions) in the natural ambient magnetic field created by the presence of the ferromagnetic material.

Non-destructive inspection methods are divided into two main groups: active and passive. A specificied external magnetic field is applied to the ferromagnetic material in the active inspection

method, and a receiver records its response. In contrast, a passive method has no actively managed external magnetic source; the residual magnetism of the specimen affects the earth's natural magnetic field, and anomalies in this field are associated with inhomogeneities and discontinuities in the ferromagnetic material (Gontarz *et al*., 2009).

The natural residual magnetic property in ferromagnetic materials results from the earth's magnetic field or the production process, and its intensity is much less than the inductive artificial magnetic property. Moreover, magnetic anomalies can reflect the stress changes in ferromagnetic materials, which are not directly related to material defects. Therefore, passive magnetic inspection method results are more complicated to analyze than active method results, and more sophisticated and sensitive devices are needed (Gontarz *et al*., 2012).

Reinforcement corrosion is a major issue in many types of reinforced concrete structures. The penetration of moisture and chloride ions into the reinforced concrete and consequent chemical reactions with the reinforcement rebar leads to deterioration (loss of cross-section) and defects (deep point corrosion) in the rebar (Zhou *et al.*, 2015). This process may also increase the corroded rebar volume (oxidation and swelling), generating cracks in the concrete and further decreasing the service life of the reinforced concrete structure by facilitating water and oxygen penetration.

Developing an obligatory structural repair work schedule requires quantification of the corrosion percentage and the distribution and location of the defects, achieved by using non-destructive or destructive inspection methods. Reliable non-destructive test methods are more desirable because of they are non-invasive, cheaper and faster in application than destructive ones.

There are limitations to each specific non-destructive assessment method. For instance, applications of electrical, electromechanical, and acoustic probing methods are limited by variations

in the moisture, salinity conditions, and inhomogeneity of concrete. These limitations even may put a halt against reinforcement assessment by such methods (Mancio *et al.*, 2004; Qian *et al.*, 2001).

Steel reinforcement is a ferromagnetic material, and magnetic corrosion detection methods like Magnetic Flux Leakage (MFL) can be used to defect detections. MFL method uses an inductive magnetic field, and so is an active non-destructive testing method (Fernandes *et al.*, 2012; Gaydecki *et al.*, 2007).

The Passive Magnetic Inspection (PMI) method is used in this thesis to gather raw magnetic data of ferromagnetic steel reinforcement (Mahbaz, S.B., 2016). The basis of the PMI method is the natural magnetic field around the steel rebar. During steel rebar manufacturing, the earth's magnetic field modifies the natural magnetic field of the steel rebar. This process is called Self Magnetic Flux Leakage (SMFL) (Wilson *et al.*, 2007), (Doubov *et al.*, 2000), (Doubov *et al.*, 1998).

A steel rebar has a unique magnetic signature arising from the stress and strain during the manufacturing process under the earth's natural magnetic field. Therefore, any reinforcement has its specific magnetic field characteristics based on the stress-strain history and manufacturing condition (Hubert *et al.*, 1998).

The magnetization process defines the anisotropic self-magnetization field of a ferromagnetic material (Vlasov *et al.*, 2004). The ambient magnetic field around any ferromagnetic material is distorted by the self-magnetized aligned electron dipoles in the iron crystallite. The ambient magnetic field is affected by crystal anisotropy (microstructure) and induced magnetization. The crystal anisotropy of ferromagnetic materials depends on their crystal structure and the induced anisotropy depends on the deviation (orientation) of electron dipoles from an initial random state.

The magnetic fields are classified into two general types: stray magnetic fields and external magnetic fields (Döring *et al.*, 1966), (Brown *et al.*, 1962), (Aharoni *et al.*, 2000). There is a relation between an external magnetic field (H) with the vacuum magnetic permeability (μ_0), magnetic flux density (B), and the magnetic polarization (J), written in Eq.2-1.

$$divB = div(\mu_0 H + J) = 0 \tag{2-1}$$

Hubert et al. (1998) presented the following equation for stray field gradient, in which H_d is referred to as the stray magnetic field (Eq.2-2):

$$divH_d = -div(J/\mu_0) \tag{2-2}$$

The stray magnetic field H_d and the energy of stray magnetic field E_d are related as follows

$$\mathrm{E_d} = \frac{1}{2}\mu_0 \int_{\text{all space}} \mathrm{H_d^2 dV} \rightarrow \mathrm{E_d} = -\frac{1}{2}\mu_0 \int_{\text{sample}} \mathrm{H_d J dV} \tag{2-3}$$

In this equation V is the volume of the element. According to potential theory, there is a solution for the stray field equation which relates magnetization (M), the value of surface charge density (σ_s=$M \cdot n$) and the volume charge density (λv).

$$\lambda_v = -div\, M \tag{2-4}$$

$$M(r) = J(r)/J_s \tag{2-5}$$

Here, $\boldsymbol{J_s}$ is the magnetization saturation and r indicates the vector of position. Two different materials with different M values (M_1, M_2) develop an interface charge:

$$\sigma_S = (M_1 - M_2)n \tag{2-6}$$

Here, n is the normal vector at the separation surface of the two materials. By combining equations 2-3, 2-4, and 2-5 and integrating over the volume at the *r* position, the potential of the stray field energy would be:

$$\Phi_d(r) = \frac{J_s}{4\pi\mu_0}\left[\int \frac{\lambda_v(r')}{|r-r'|}dV' + \int \frac{\sigma_s(r')}{|r-r'|}dS'\right] \quad (2\text{-}7)$$

where r', V', and S' are the derivatives of r, V, and S respectively. Using Eq.(**2-7**) the stray field can be calculated as follows:

$$H_d(r) = -grad\Phi_d(r) \quad (2\text{-}8)$$

The stray field energy is calculated as follows:

$$E_d = J_s[\int \lambda_v(r)\Phi_d(r)dV + \int \sigma_s(r)\Phi_d(r)dS] \quad (2\text{-}9)$$

Any defects in ferromagnetic specimens lead to a change in the stray energy value. Schneider *et al.* (2001) stated that the arrangement of smaller domains, which altered the magnetic domain of walls by denser aligned dipoles, is the basis for a change in stray field energy. In this thesis, the changes in the stray field energy as a reliable method to assess the domain changes are used to simulate the relation between magnetic flux density and defects on ferromagnetic specimens.

2.1 Wavelet

The PMI method provides non-stationary, two dimensional signals of magnetic flux density value versus time or location. The time-frequency functions provide information on the frequency and time content of a signal simultaneously. Therefore, are suitable to transform non-stationary data like PMI. Wavelets are a particular type of function, mainly a basis function, localized in both time and

frequency. The wavelet function, or "mother" wavelet (ψ), which defines the basic wavelet shape, typically defines wavelets. There are different wavelet functions with different properties (Fugal, 2009) (Figure **2-1**).

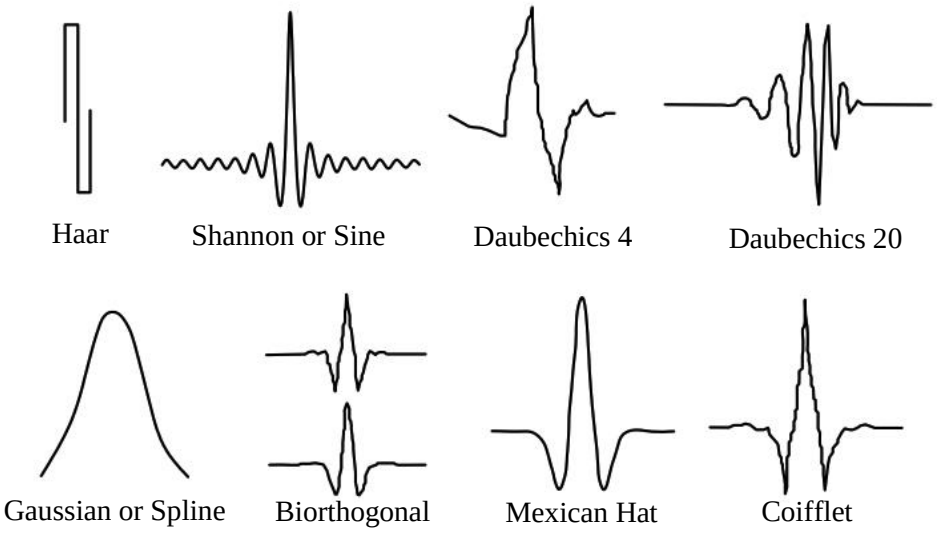

Figure 2-1: Some wavelet functions

The wavelet function creates an entire family of wavelets according to 2-10:

$$\psi_{j,k}(t) = 2^{\frac{j}{2}}\psi\left(2^j t - k\right) \quad j \; and \; k \in \mathbb{Z} \tag{2-10}$$

where (j) is dilation index or scale factor and (k) is translation index or shift factor (Ogden, 1997). A linear combination of these dilated and translated mother wavelet functions can represent a signal. Wavelet function has a useful property called wavelet decomposition, discussed in the next section.

2.1.1 Wavelet decomposition

Wavelet has a useful property of separating low and high-frequency content of a signal, called decomposition of a signal. Wavelet decomposition breaks up a signal into a low-frequency approximation using a scaling function ($\phi_{j,k}$) and high-frequency signal content by the wavelet function ($\psi_{j,k}$). A signal $s(t)$ can be decomposed into an approximation component and a detail component. The approximation component is defined by scaling functions, and the rest of the signal is described by wavelet functions (Burrus *et al.*, 1998) (Eq.2-11).

$$s(t) = \sum_k c_{j,k}\phi_{j,k}(t) + \sum_k d_{j,k}\psi_{j,k}(t) \qquad 2\text{-}11)$$

Therefore, a signal can be decomposed until a specific detail of resolution is achieved. For instance, for level *j=3* of approximation (A_j) and signal detail (D_j) the signal $s(t)$ is defined according to Eq.2-12 (

Figure **2-2**):

$$s(t) = A_3 + \sum_{j=1}^{3} D_j \qquad (2\text{-}12)$$

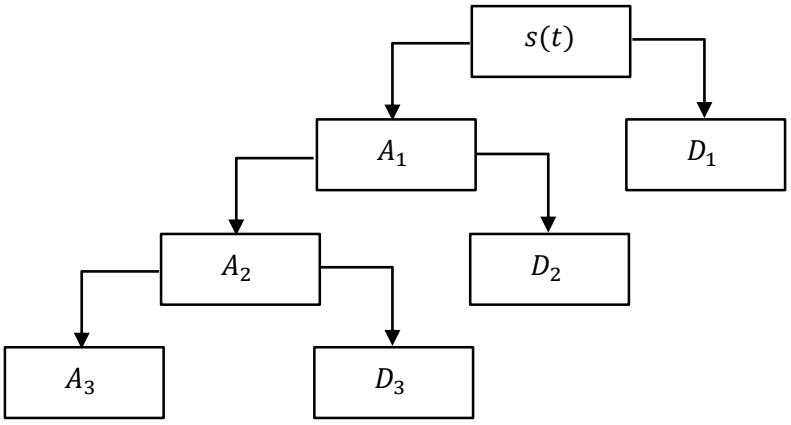

Figure 2-2: Wavelet decomposition sequence (Misiti *et al.* 1997)

Considering j as the level of resolution, the signal approximation $A_j(t)$, and the signal details $D_j(t)$ are defined by scaling and wavelet functions (Burrus *et al.*, 1998) (Ogden *et al.*, 1997):

$$A_j(t) = \sum_k c_{j,k}\phi_{j,k}(t) \tag{2-13}$$

$$D_j(t) = \sum_k d_{j,k}\psi_{j,k}(t) \tag{2-14}$$

This decomposition property of the wavelet function is used in this thesis to detect corrosion in steel reinforcement.

2.2 Steel rebar corrosion assessment using wavelet decomposition

Choosing the appropriate level of decomposition (Eq. 2-12) and selection of wavelet transform play essential roles in detecting rebar defects effectively. In this thesis, the Haar wavelet decomposition is selected to detect corrosion in the steel reinforcement. More specifically, this thesis develops an analysis of embedded concrete steel reinforcement magnetic data with the wavelet decomposition using MATLAB™ software.

2.2.1 Haar wavelet decomposition

The Haar wavelet function for $x \in [a, b)$ is defined in Eq.(2-15) (Liu *et al.*, 2021).

$$h_i(x) = \begin{cases} 1 & for \quad x \in [\xi_1, \xi_2) \\ -1 & for \quad x \in [\xi_2, \xi_3) \\ 0 & Elswhere \end{cases} \tag{2-15}$$

Where

$$\xi_1 = a + (b-a)\frac{k}{m}$$

$$\xi_2 = a + (b-a)\frac{k+0.5}{m}$$

$$\xi_3 = a + (b-a)\frac{k+1}{m}$$

$$m = 2^j, j = 0,1,\dots,J$$

$$k = 0,1,\dots,m-1$$

The j parameter represents the wavelet's level, J is the maximum resolution level, and k is the translation parameter.

The Haar wavelet is a mathematical function with a wide variety of applications, like the approximation of the linear homogeneous and linear non-homogeneous aspects of Klein–Gordon equations (Ikram *et al.*, 2021), the free vibration analysis of combined functionally graded shells (Kim *et al.*, 2021), and finding a feature extraction method based on geometric features and the Haar wavelet.

The Haar wavelet function, level three of signal detail, is used to detect rebar defects in this work. Data analysis based on absolute Gradient Values (AG) (Mosharafi, 2020) is used to verify the Haar wavelet detection results. The SMFL sample signal (Figure 2-3) is gathered using the PMI device by scanning specific embedded rebar in the Toogood Pond Dam, Markham, Ontario (Figure 2-4), and the raw magnetic signal is analyzed with the Haar wavelet and AG method for verification.

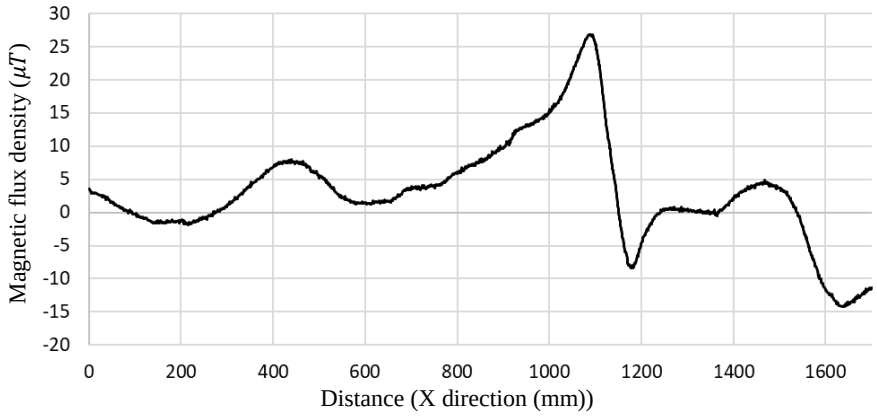

Figure 2-3. Sample SMFL signal

Figure 2-4. Toogood Dam sample rebar

The AG analysis shows one major corrosion site at length 1150mm, and three minor corrosion sites at 1050mm, 1200mm, and 1580mm length of the embedded rebar (Figure 2-5).

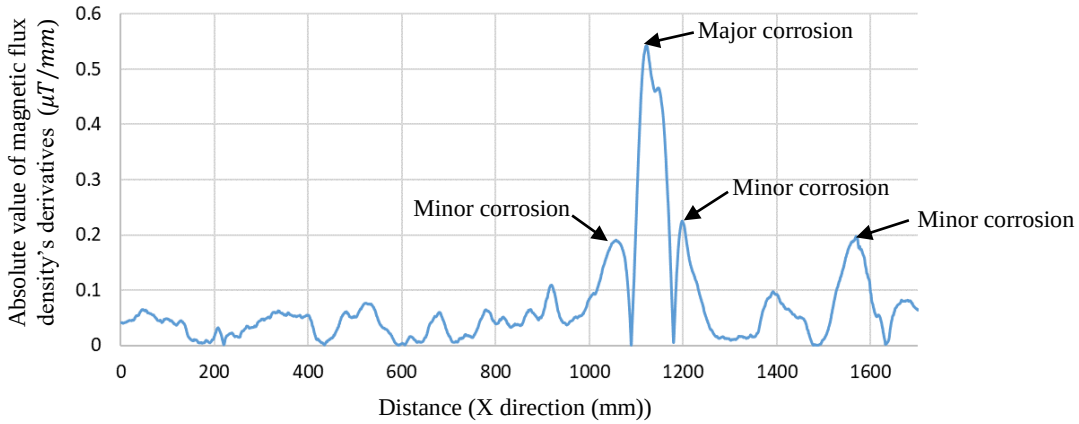

Figure 2-5. AG corrosion analysis result

MATLAB™ software is used for the Haar wavelet analysis. The sample SMFL signal is decomposed into one approximation signal and three detailed signals. Each level of the detailed signals is calculated by decomposition of the previous level of approximation signal (

Figure **2-2**). The following image shows the approximation signal and three detailed signals of the sample rebar of Toogood Pond Dam. The addition of these signals constructs the sample signal (Eq. 2-12).

(a)

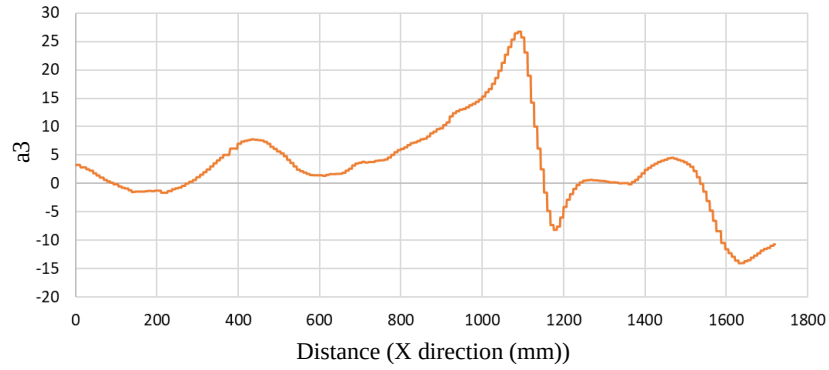

(b)

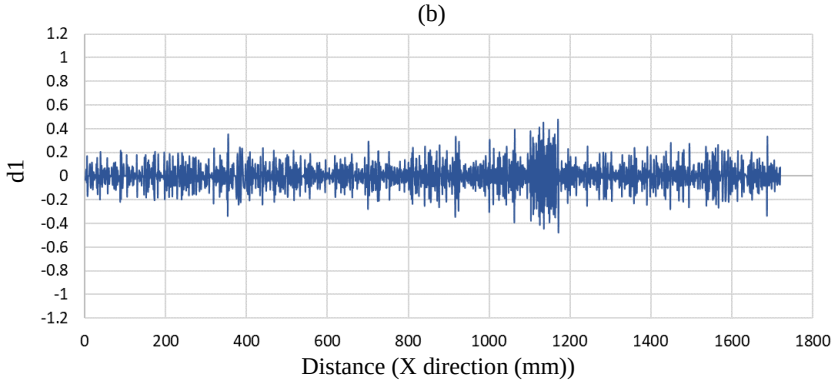

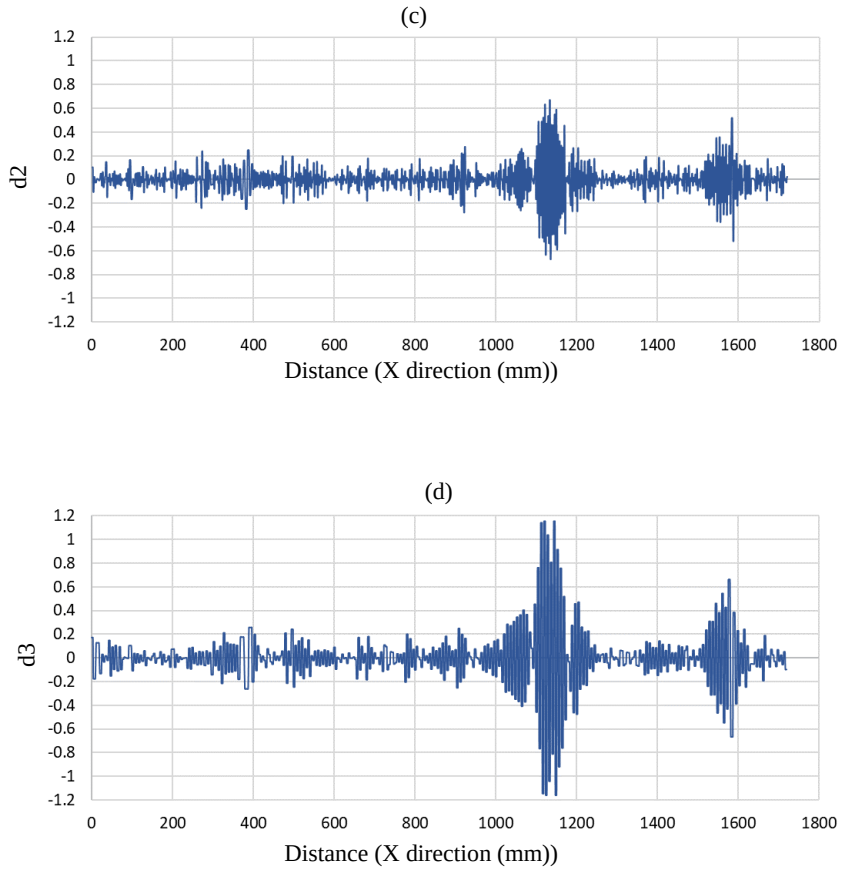

Figure 2-6. Haar wavelet level three decomposition results of Toogood Dam sample rebar. (a) Level three of approximation signal. (b) Level one of detailed signal. (c) level two of detailed signal. (d) level three of detailed signal.

The results show that the level three signal details have good compatibility with the AG corrosion detection method (Figure 2-7). The AG method resulted in a signal maximum value of 0.53, and the Haar wavelet analysis maximum value is 1.15. Using the scale factor 0.53/1.15, the Haar wavelet analysis signal illustrates clear compatibility with the AG analysis results. The Haar wavelet detailed signal is symmetric with respect to Y axis. Therefore, the negative part is deleted for more clarity (Figure 2-8).

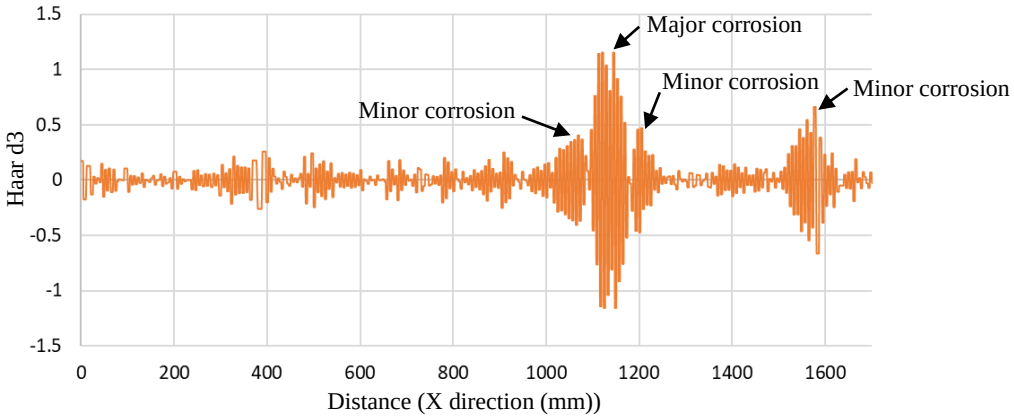

Figure 2-7. Haar wavelet d3 analysis result

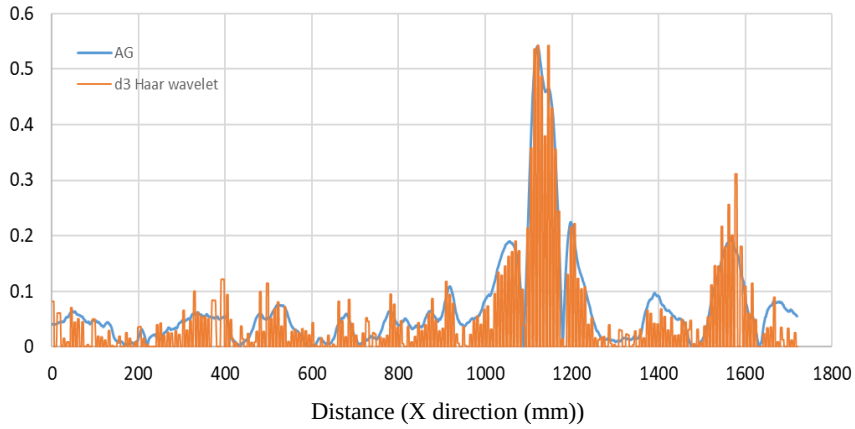

Figure 2-8. Comparison between AG analysis and Haar wavelet analysis results

The correlation coefficient is used for quantifying the similarity between the signals. In general, the Haar detailed signal has an up-and-down shape in each cycle (Figure 2-1). Therefore, the maximum adjacent points of each cycle are connected to each other to reach a smooth curve and allow the correlation coefficient calculation. The correlation coefficient between AG and the Haar wavelet signals is 0.96, which shows high compatibility between the resulted signals. It should be

noted that although the correlation coefficient shows that the two signals are very similar, detection of the corrosion points location and amplitude are the main goals of these two detection methods. The location of major corrosion and the amplitude of the pulses are the same in two AG and Haar wavelet methods (Figure 2-9).

The Toogood Pond Dam piers rebar corrosion is assessed using the Haar wavelet method the results compared with the AG method results. The details are presented in the next chapter.

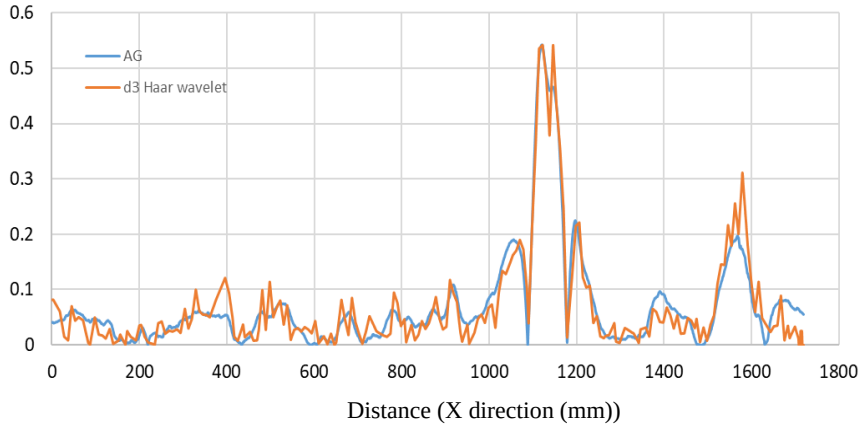

Figure 2-9. Comparison between AG analysis and Haar wavelet analysis results (smoothed curve)

Chapter 3

Toogood Pond Dam, The Case Study

3.1 Introduction

The PMI method concept is presented in Chapter 2, and the wavelet ability in the signal decomposition is also explained in Section 2.2. In this chapter, the corrosion of the concrete reinforcement of a dam is assessed using the PMI method and wavelet analysis, and the results are verified with the available reinforcing steel rebar corrosion assessment method. In this research, the Toogood Dam reinforcement was assessed as a case study. Inspections focused on the lower half of each section since these areas are subjected to higher environmental impacts because of moisture and water flow and are therefore expected to have a higher amount of corrosion. For the Toogood Dam reinforcement assessment, rebar location and orientation were delineated first. Next, the SMFL values of the detected steel reinforcement were recorded using PMI technology. Subsequently, the wavelet decomposition was used for the interpretation of recorded magnetic dataset values and rebar corrosion detection. Finally, results were compared to the AG method as the other rebar reinforcement detection corrosion methods for verification.

3.2 Site description

Toogood Dam creates the Toogood Pond located in the Rouge River Watershed downstream of the confluence of Bruce Creek and Berczy Creek. The watershed area is around 7300 ha in total and

continuous northward to include Preston Lake in Whitchurch Township. The pond area is about 3 ha (Figure 3-1).

Figure 3-1. Toogood Pond Dam location

Reports indicate that the Toogood Pond was formed by a dam in 1960 (Toogood Correspondence, 1980). The presently visible concrete structure was built in 1981 on top of the existing structure to serve recreational purposes. The dam is made up of a 23 m long, about 6 m high concrete spillway, including five stop log bays with earth embankments on each side. The dam includes four concrete bearing piers and two embankments. The dam's embankments have concrete walkways fixed overtop to provide a continuous walkway across the dam. The embankments have interconnected concrete segments on the surface, and the dam also has an excavated channel and culvert crossing through it to give fish passage (Figure 3-2).

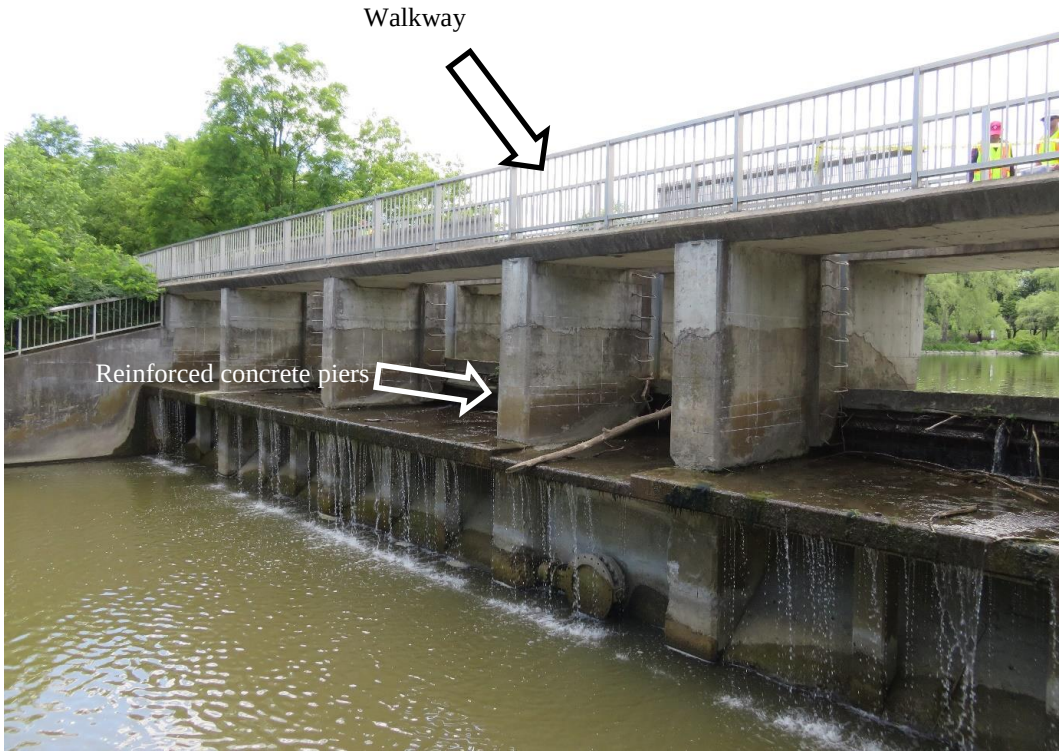

Figure 3-2. Toogood Pond Dam structure - South to North view

3.3 PMI data gathering

The wet dam environment makes the concrete dam prone to electrochemical corrosion. The corrosion condition of embedded reinforcement rebars of the Toogood Dam was assessed using the PMI method. The two sides of the four bearing piers plus the exposed sides of the concrete embankments were inspected. The ten inspected areas are shown in Figure 3-3.

The inspection started with detecting the location and the orientation of the reinforcement in all ten areas using an industrial rebar detector –Bosch D-Tect 150 (Figure 4-4 (a)). Then, the detected rebar location was marked with a visible marker on each area (Figure 4-4 (b)). Three horizontal rebars

and two vertical rebars were marked on each area to be scanned with a PMI technology scanner (Figure 3-4 (c)). The start and the end points' location of the marked rebar lines were accurately documented.

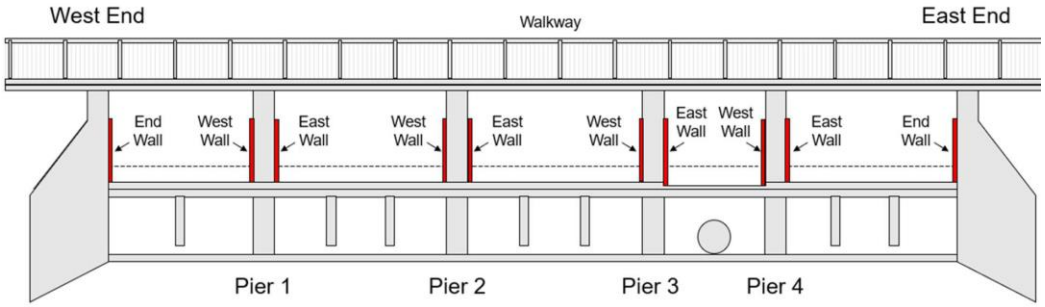

Figure 3-3. Inspected areas on the bearing piers sides and two embankments

(a)

(b)

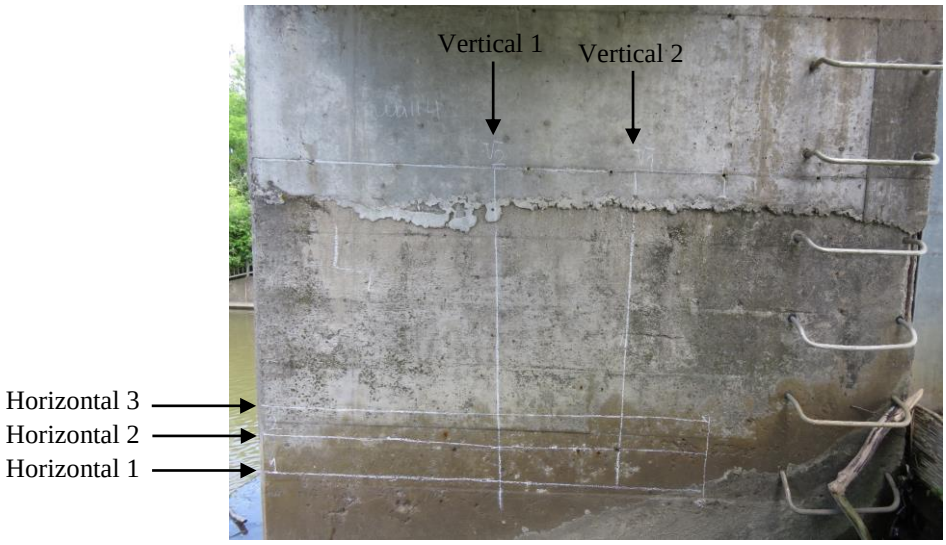

(c)

Figure 3-4. (a) Detecting rebar location; (b) Marking the detected rebar location on each concrete area; (c) Three horizontal and two vertical detected rebar

In the next step, the PMI scanner moved over 50 marked paths with a constant speed to gather raw magnetic data (Figure 3-5). All raw magnetic data was saved in the PMI scanner's SD card and uploaded on the computer for analysis.

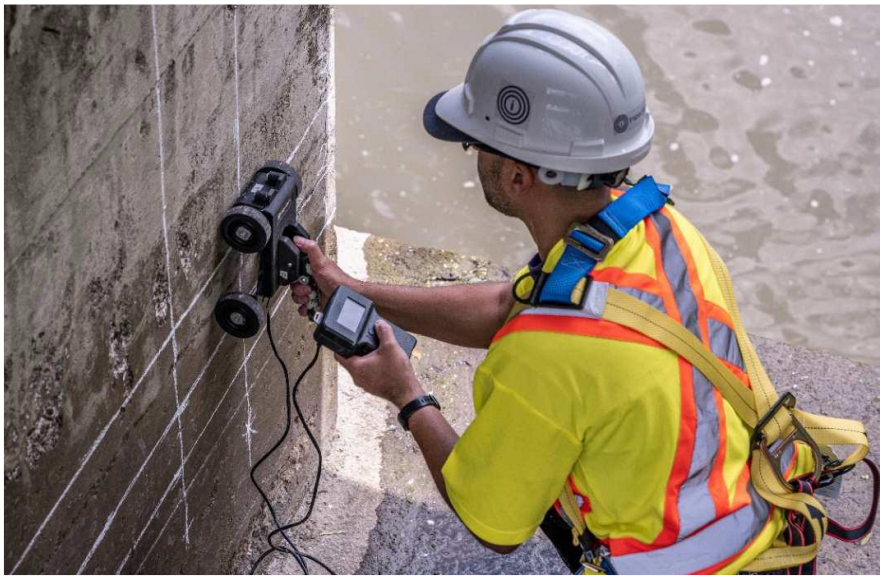

Figure 3-5 Scanning the raw magnetic data using the PMI device

3.4 PMI inspection results using wavelet analysis

In the ferromagnetic reinforcement inspection method, any changes in the magnetic-domain properties are considered a defect (Wang *et al.*, 2012). Different reasons may lead to changes in the magnetic domain of ferromagnetic materials such as stress concentrations, cracking, fatigue, and corrosion. Therefore, the magnetic-domain change locations may include one or a combination of rebar defect types. Three approximate categories based on the rebar area loss are considered for establishing future maintenance plans:

- The cross-section area loss 4-7% is considered the upper limit for small defects.
- The cross-section area loss 7-10% is considered the range for moderate defects.
- The cross-section area loss greater than 10% is considered the lower limit for major defects.

PMI magnetic data of each wall are analyzed using the Haar wavelet analysis and then compared with AG analysis methods for verification. The similarity between the AG method result and the Haar wavelet decomposition method result is controlled visually and quantified with correlation coefficients.

3.4.1 End west wall

The wall is located on the west dam embankment. The wall and five scanned paths are shown in Figure 3-6 and the positive direction of the PMI scanner movement is shown with the red lines.

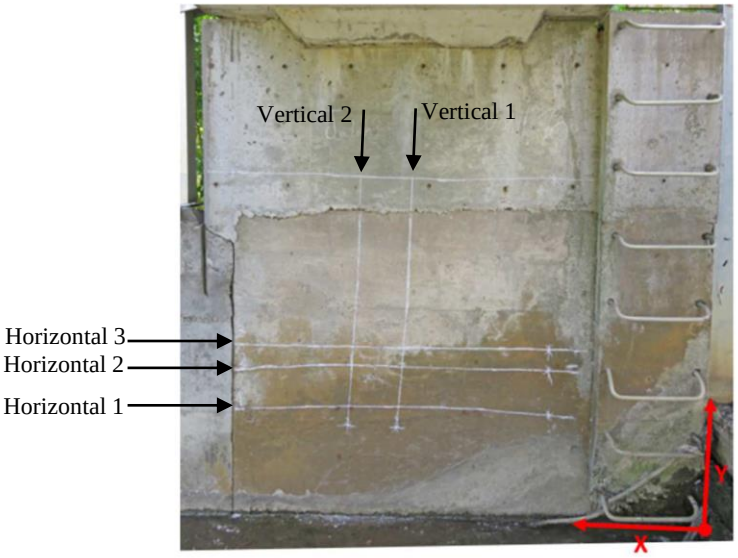

Figure 3-6. End west wall

The AG method results show the maximum corrosion equals 7% in the Horizontal 1 rebar. The location of maximum rebar corrosion in the Horizontal 2 rebar is the same as Horizontal 1. The

maximum corrosion in Horizontal 3, Vertical 1, and Vertical 2 are 5%, 3%, and 7%, respectively (Figure 3-7).

The Haar wavelet analysis predicted the location and amplitude of all areas with cross-sectional losses greater than 4% in horizontal and vertical rebars accurately. Horizontal 1 has two areas with loss greater than 4% at 380mm and 420mm distance, Horizontal 2 area loss greater than 4% occurs at 380mm distance, and Horizontal 3 area loss greater than 4% area loss occurs at 1550mm distance, all predicted with high accuracy by the Haar wavelet. The quality of detection of the point with area loss greater than 4% is high for the vertical rebars too.

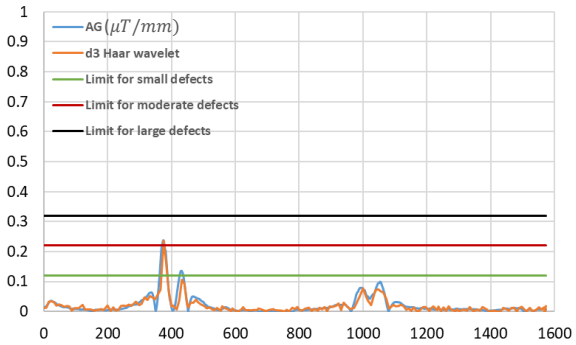

(a)

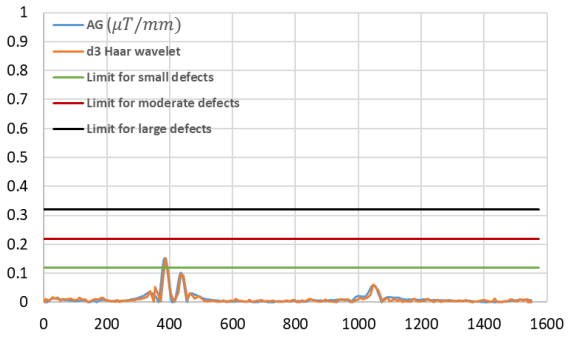

(b)

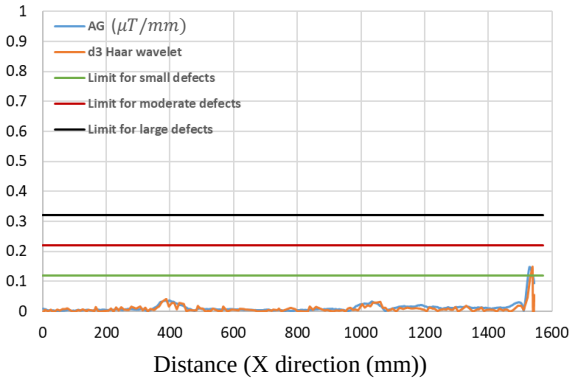

(c)

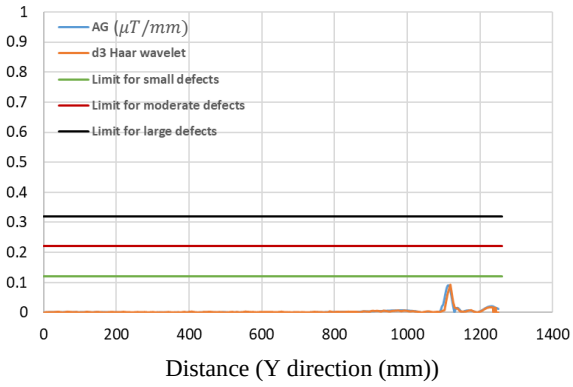

(d)

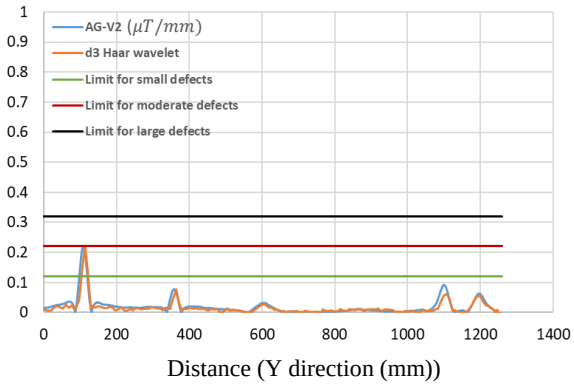

(e)

Figure 3-7. End west wall AG method and Haar wavelet analysis results. (a) Horizontal 1. (b) Horizontal 2. (c) Horizontal 3. (d) Vertical 1. (e) Vertical 2.

The correlation coefficients between AG and Haar wavelet signals are presented in Table 1. All coefficient values are higher than 0.8, and the highest value is 0.94. There are some fluctuations in the d3 Haar wavelet of Horizontal 3 rebar, which decreased the correlation coefficient. However, the location of the area of losses is detected accurately (Figure 3-7 (c)).

Table 1-Correlation coefficient between the AG and the Haar wavelet signals of the end west wall

Rebar	Horizontal 1	Horizontal 2	Horizontal 3	Vertical 1	Vertical 2
Correlation coefficient	0.94	0.92	0.83	0.90	0.93

3.4.2 Pier one-west wall

The wall is located on the west side of pier one. Five rebar paths were scanned using the PMI device, and the raw magnetic data were recorded. The PMI device moved along the given paths in the X and Y positive directions, which are marked with the red lines in Figure 3-8.

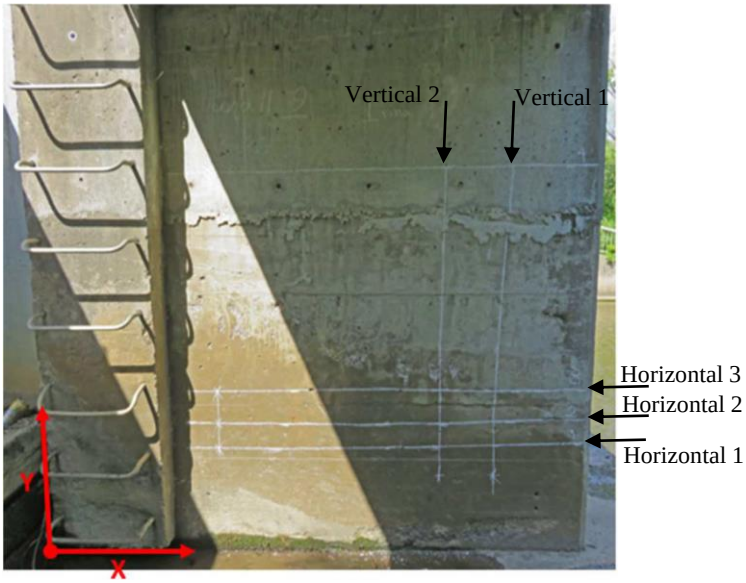

Figure 3-8. Pier one-west wall horizontal and vertical scanned paths

According to the AG method results the maximum corrosion is 7% in the Horizontal 1 and Vertical 1 rebars. The Haar wavelet analysis shows good similarity with the AG method results (Figure 3-9), and the corrosion locations (the pulses in the AG method) are in general detected correctly with the Haar wavelet method. According to the AG method, Horizontal 1 has two small defects at 1050mm and 1650mm distances. The Haar wavelet method predicted the location of these corrosion points accurately. However, there is some difference in the corrosion value (Figure 3-9 (a)). The AG and the Haar wavelet give the location and amplitude of defects almost the same in Horizontal 2 and Horizontal 3 rebars (Figure 3-9 (b) and (c)). Vertical 2 rebar has three points with cross-setional area loss between 4 and 7% at the 800mm, 1080mm, and 1120mm distances. The Haar wavelet upper estimated the first one and underestimated two other points.

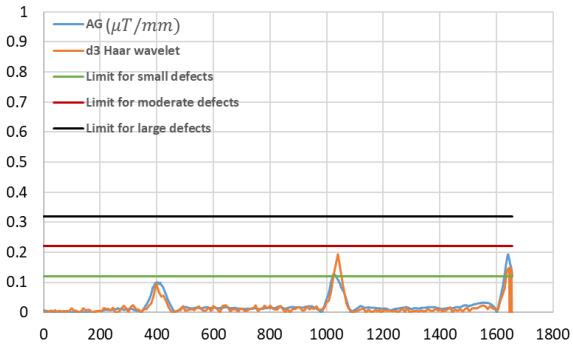

Distance (X direction (mm))

(a)

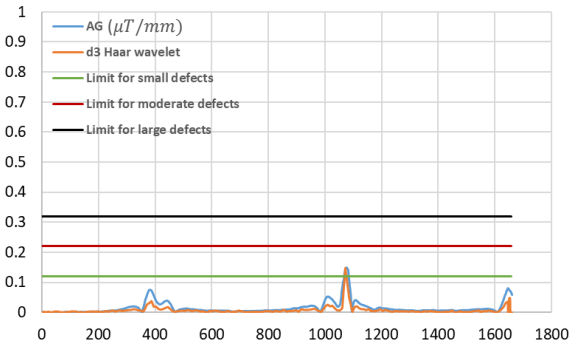

Distance (X direction (mm))

(b)

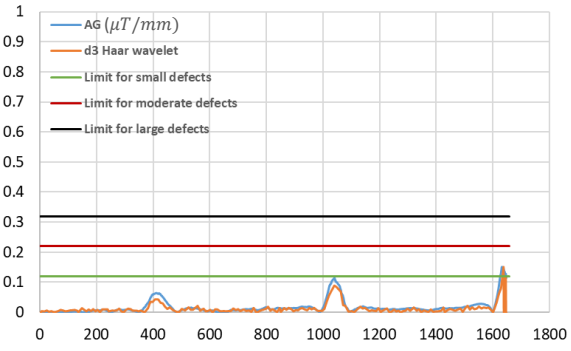

Distance (X direction (mm))

(c)

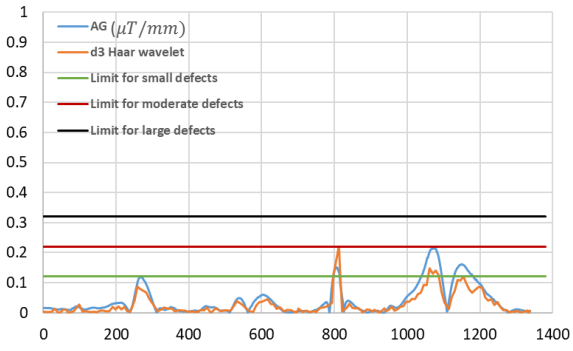

Distance (Y direction (mm))

(d)

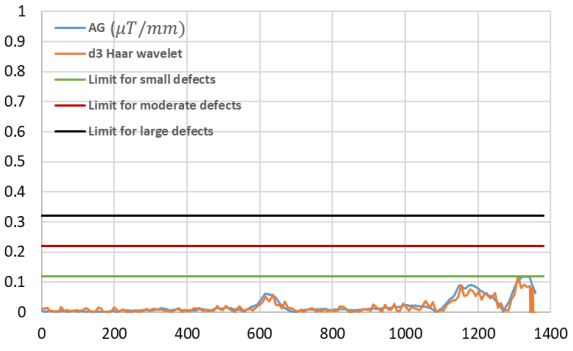

Distance (Y direction (mm))

(e)

Figure 3-9. Pier one- west wall AG method and Haar wavelet analysis results. (a) Horizontal 1. (b) Horizontal 2. (c) Horizontal 3. (d) Vertical 1. (e) Vertical 2.

All the correlation coefficients values between AG method signals and the Haar wavelet are higher than 0.85 (Table 2). Although the Haar wavelet method detected the corrosion points correctly, there are some differences between the amplitude of the signals at the corrosion points, which decreased the correlation coefficient.

Table 2-Correlation coefficient between the AG and the Haar wavelet signals of the pier one west wall

Rebar	Horizontal 1	Horizontal 2	Horizontal 3	Vertical 1	Vertical 2
Correlation coefficient	0.85	0.88	0.89	0.95	0.91

3.4.3 Pier one - east wall

The wall is the east part of pier one. The five PMI scanned paths and the direction of positive X and Y PMI device movement direction are shown in Figure 3-10.

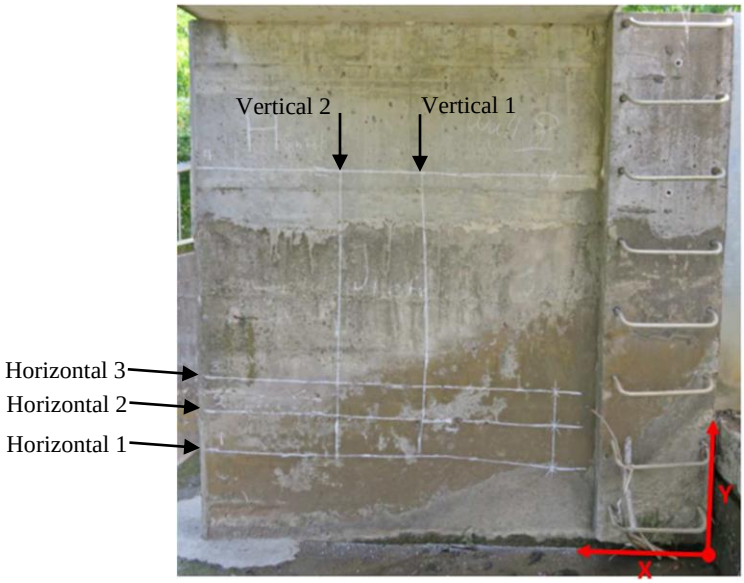

Figure 3-10. Pier one - east wall horizontal and vertical scanned paths

The AG method shows the maximum area loss in this wall's rebars is 6%, in the Horizontal 1, Horizontal 2, and Horizontal 3. The Haar wavelet method detected all these corrosion points accurately (Figure 3-11 (a), (b), and (c)). Although the defects in the vertical rebars are less than the limit for small defects, minor pulses of the AG method and the Haar wavelet method are identical (Figure 3-11 (d) and (e)).

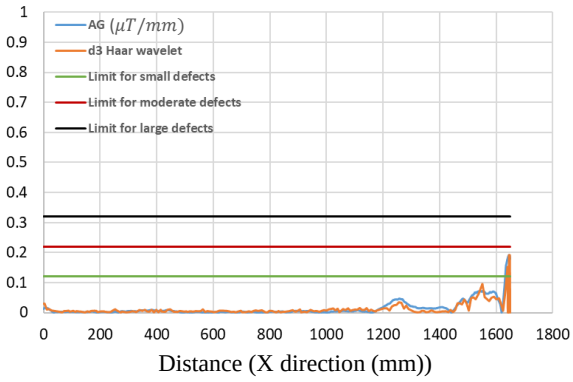

(a)

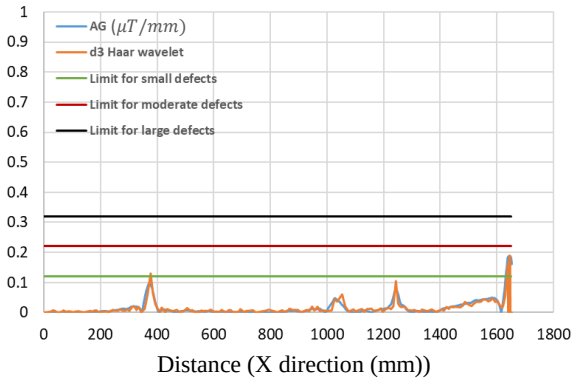

(b)

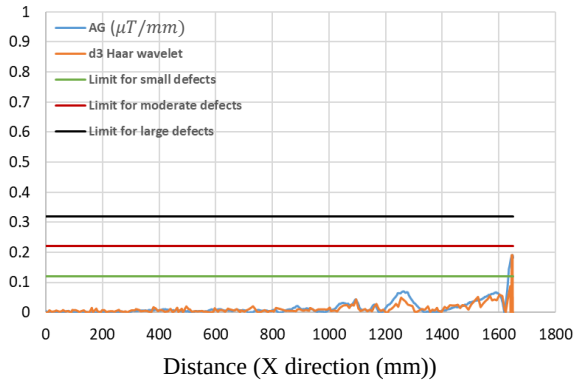

(c)

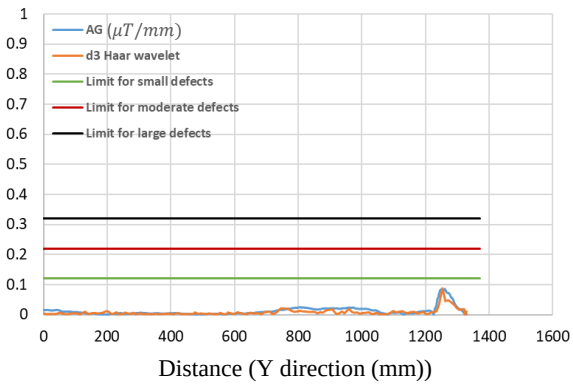

(d)

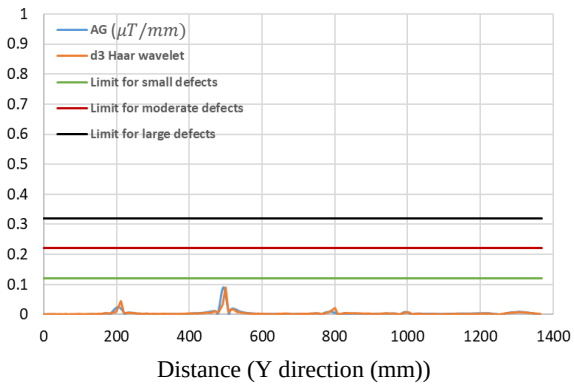

(e)

Figure 3-11. Pier one- east wall AG method and Haar wavelet analysis results. (a) Horizontal 1. (b) Horizontal 2. (c) Horizontal 3. (d) Vertical 1. (e) Vertical 2.

The correlation coefficient shows the similarity between AG signals and Haar wavelet signals is in the 0.75 to 0.85 range (Table 3). Horizontal 2 and Horizontal 3 show the lowest correlation coefficient because of the fluctuations in the Haar wavelet resulted signal.

Table 3-Correlation coefficient between the AG and the Haar wavelet signals of the pier one east wall

Rebar	Horizontal 1	Horizontal 2	Horizontal 3	Vertical 1	Vertical 2
Correlation coefficient	0.84	0.76	0.75	0.86	0.85

3.4.4 Pier two- west wall

Three horizontal and two vertical scanned rebars with the PMI scanner on the west wall of pier two are shown in Figure 3-12. The positive directions of the PMI device movement are marked with the red axes.

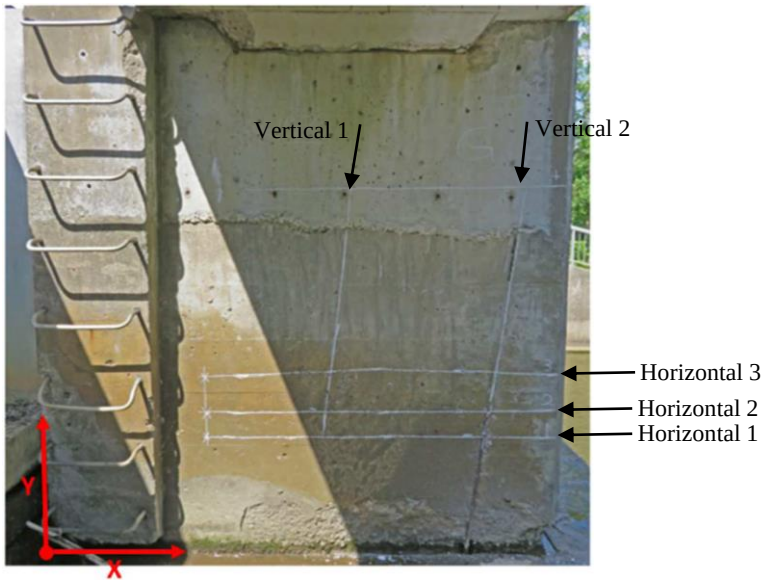

Figure 3-12. Pier two - west wall horizontal and vertical scanned paths

Maximum corrosion in the rebars of this wall is 15%. The Haar wavelet analysis detected location of all pulses in AG signals (corrosion points) correctly (Figure 3-13). For the Horizontal rabars, the Haar wavelet simulates the value of the rebar corrosion with high accuracy. The detected corrosion at the end of the Vertical 2 rebar by the Haar wavelet is less than the AG method (Figure 3-13 (e)).

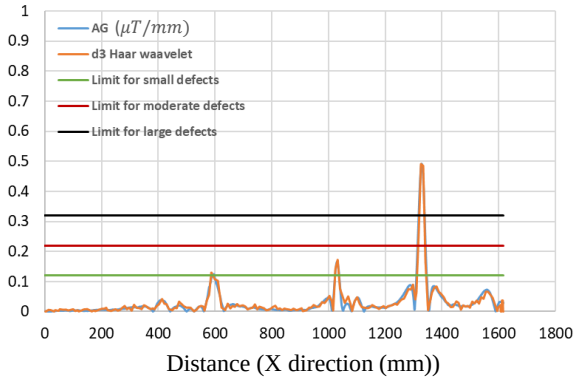

(a)

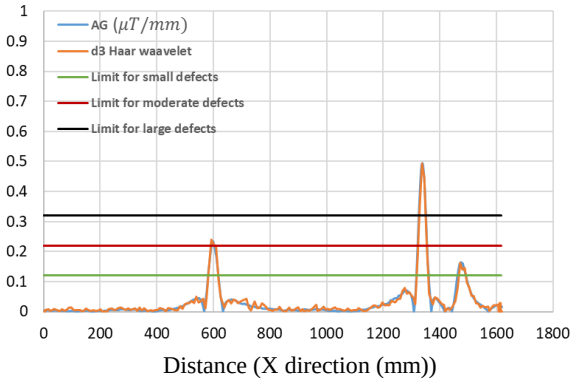

(b)

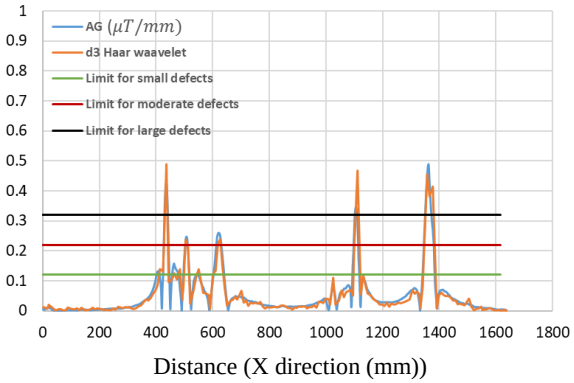

(c)

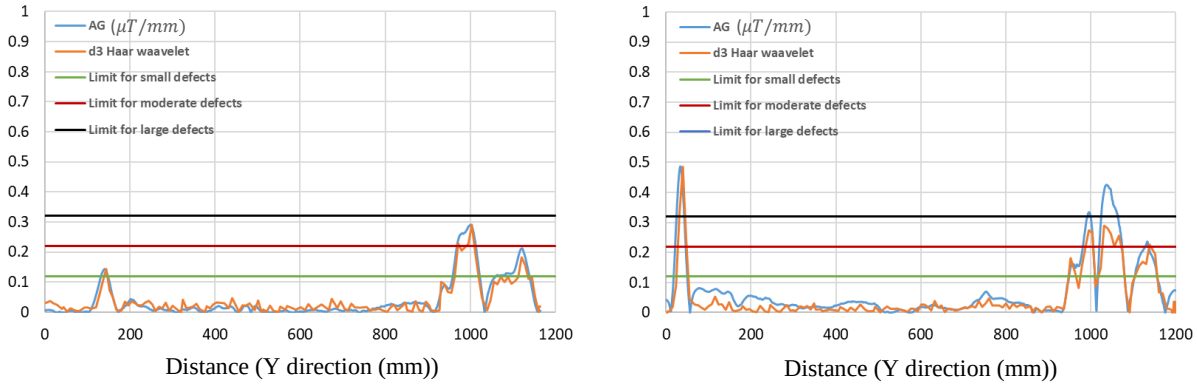

Figure 3-13. Pier two - west wall AG method and Haar wavelet analysis results. (a) Horizontal 1. (b) Horizontal 2. (c) Horizontal 3. (d) Vertical 1. (e) Vertical 2.

Correlation coefficient values demonstrate a high value of similarity between AG and Haar wavelet results for this wall. The minimum coefficient value is 0.95, and the maximum is 0.99 (Table 4).

Table 4-Correlation coefficient between the AG and the Haar wavelet signals of the pier two west wall

Rebar	Horizontal 1	Horizontal 2	Horizontal 3	Vertical 1	Vertical 2
Correlation coefficient	0.98	0.99	0.95	0.97	0.94

3.4.5 Pier two - east wall

Five selected rebars of the pier two east wall were scanned with a PMI device, and magnetic raw data were transferred to the computer for analysis. The selected rebars' paths and the positive movement direction of the PMI device are shown in Figure 3-14.

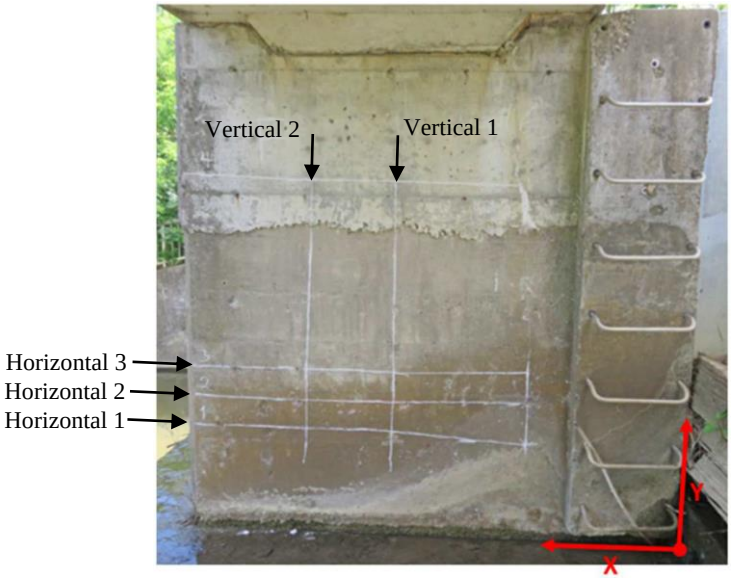

Figure 3-14. Pier two-east wall horizontal and vertical scanned paths

The Haar wavelet analysis detected two major corrosion sites between distances 1100mm and 1200mm in the Horizontal 1 rebar, Figure 3-15 (a). According to the AG analysis results there are no defective points in Horizontal 2 rebar, and the Haar wavelet results give the same results as well. However, there are some discrepancies between AG and Haar wavelet results (Figure 3-15 (b)). The AG analysis shows two major corrosion sites in the Horizontal 3 rebar between distances 1000mm to 1200mm, which are accurately captured by the Haar wavelet method (Figure 3-15 (c)). There is no cross-sectional area loss higher than 4% in Vertical 1, and Vertical 2 rebars, which is compatible with the Haar wavelet results (Figure 3-13 (c) and (d)).

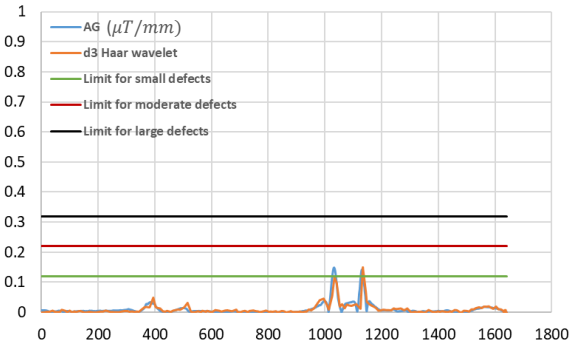

(a)

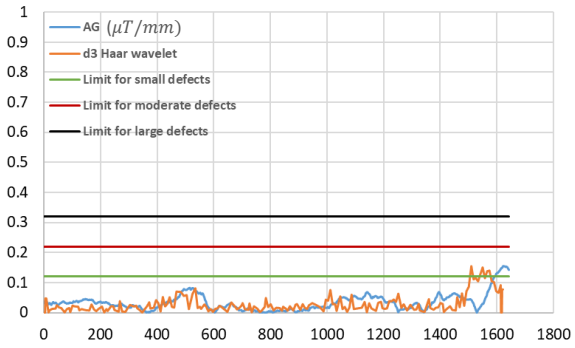

(b)

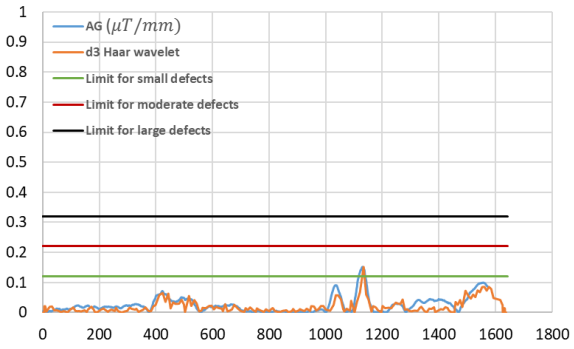

(c)

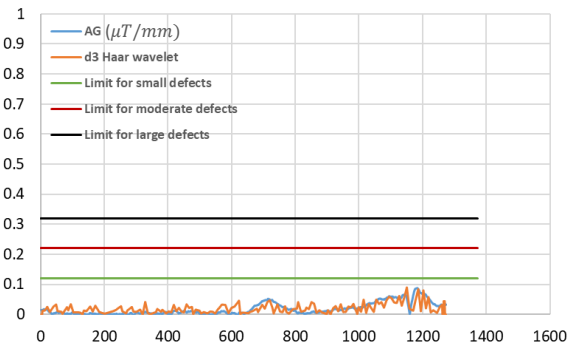

(d)

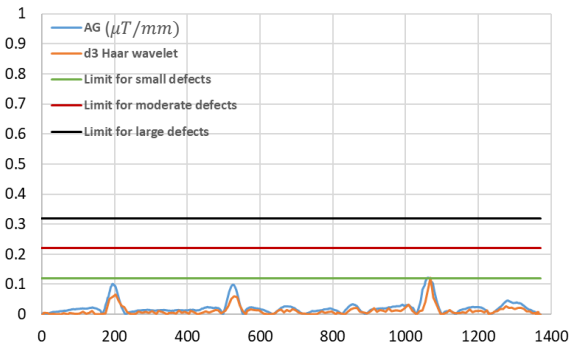

(e)

Figure 3-15. Pier two- east wall AG method and Haar wavelet analysis results. (a) Horizontal 1. (b) Horizontal 2. (c) Horizontal 3. (d) Vertical 1. (e) Vertical 2.

The correlation coefficients between AG and the Haar wavelet signals are between 0.90 and 0.66 (Table 5). The higher similarity between AG and the Haar wavelet results took place in Vertical 1 rebar resulted signals and the lower one comes from Vertical 2 resulted signals.

Table 5-Correlation coefficient between the AG and the Haar wavelet signals of the pier two east wall

Rebar	Horizontal 1	Horizontal 2	Horizontal 3	Vertical 1	Vertical 2
Correlation coefficient	0.88	0.77	0.82	0.66	0.90

3.4.6 Pier three - west wall

Five selected rebars paths are canned with the PMI scanning device and the raw magnetic data are recorded and analyzed. The selected rebars and the positive movement direction of the PMI scanner are shown in Figure 3-16.

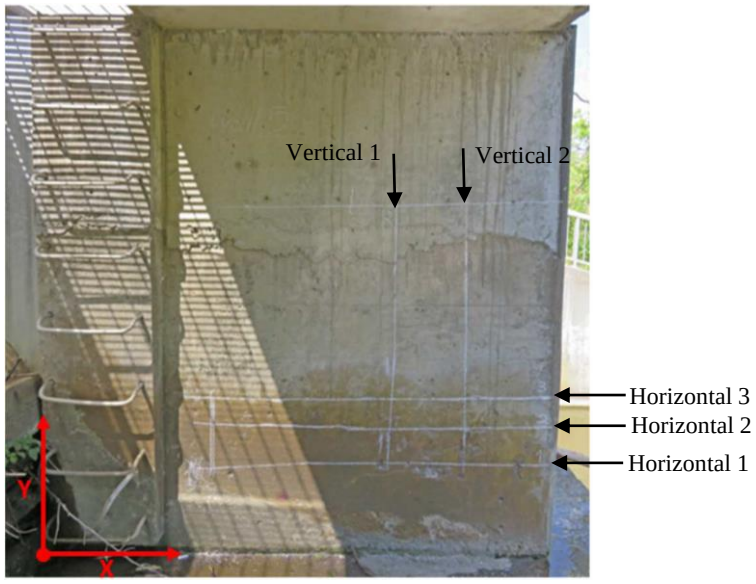

Figure 3-16. Pier three - west wall horizontal and vertical scanned paths

The AG analysis demonstrates the area loss in Horizontal 1 rebar to be less than 4%, which is similar to the Haar wavelet results. However, according to the AG analysis, the major corrosion in this rebar took place at a distance of 400mm, and the Haar wavelet analysis shows it at the distance of 200mm (Figure 3-17 (a)). There are two 5% areas loss in Horizontal 2 rebar at 400mm and 500mm distances that the Haar wavelet analysis detected corretly. However, the Haar wavelet underestimated the area loss at 500m distance as 1% (Figure 3-17 (b)). Although the Haar wavelet does not match the AG results, the Haar wavelet and AG results show the area loss in the Horizontal 3 rebar is less than 4% (Figure 3-17 (c)). The major area loss value in the 1250mm distance is detected with the Haar wavelet analysis accurately in the vertical rebars (Figure 3-17 (d) and (e)) .

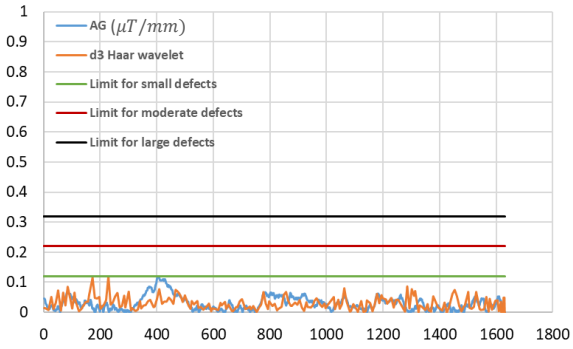

(a)

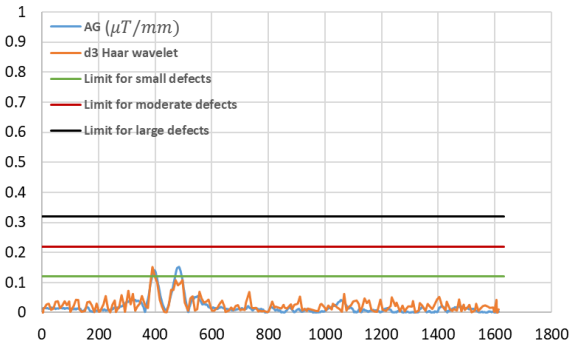

(b)

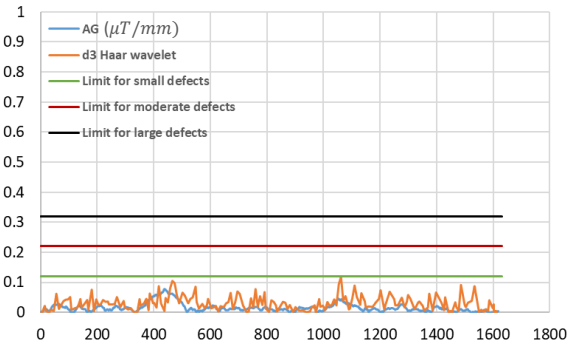

(c)

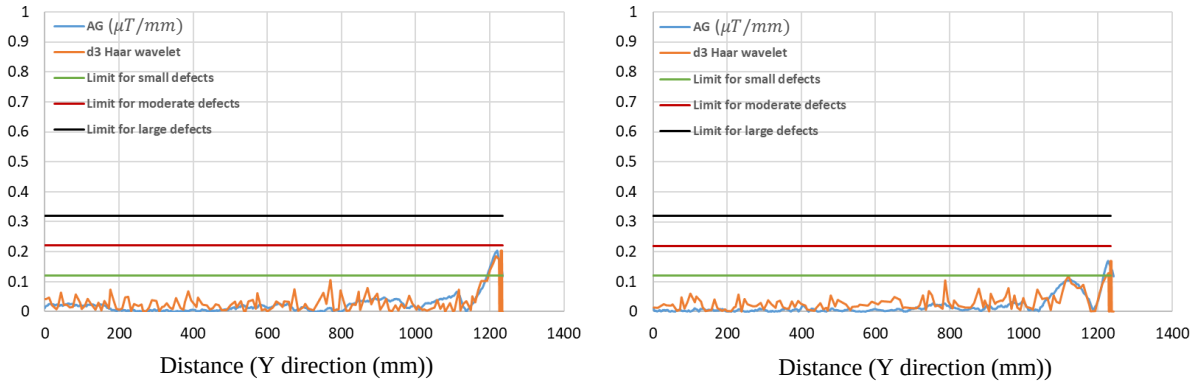

(d) (e)

Figure 3-17. Pier three - west wall AG method and Haar wavelet analysis results. (a) Horizontal 1. (b) Horizontal 2. (c) Horizontal 3. (d) Vertical 1. (e) Vertical 2.

The similarity between the Haar wavelet and AG signals are shown in Table 6. Horizontal 1 does not have any area loss larger than 4% and demonstrates lower similarity between the AG and the Haar wavelet signals. Horizontal 2 rebar has two pulses in the AG signal and 0.79 as the correlation coefficient. Although the similarity between the AG and the Haar wavelet signals is not too high for Vertical 1 and Vertical 2 signals, the amplitude and the location of the pulses are predicted accurately.

Table 6-Correlation coefficient between the AG and the Haar wavelet signals of the pier two east wall

Rebar	Horizontal 1	Horizontal 2	Horizontal 3	Vertical 1	Vertical 2
Correlation coefficient	0.17	0.79	0.40	0.72	0.67

It is important not to be confused by the low correlation coefficients in this case and in other cases. When there are strong defects that yield a strong signal, far above the background variations

("noise"), the correlation coefficients will be high. When the defects are small and yield a signal that is only moderate in amplitude compared to the background signal amplitude, one must expect the correlation coefficients to be low, as is the case here.

3.4.7 Pier three - east wall

Horizontal and vertical scanned paths and the positive direction of the PMI scanner movement are shown in Figure 3-18.

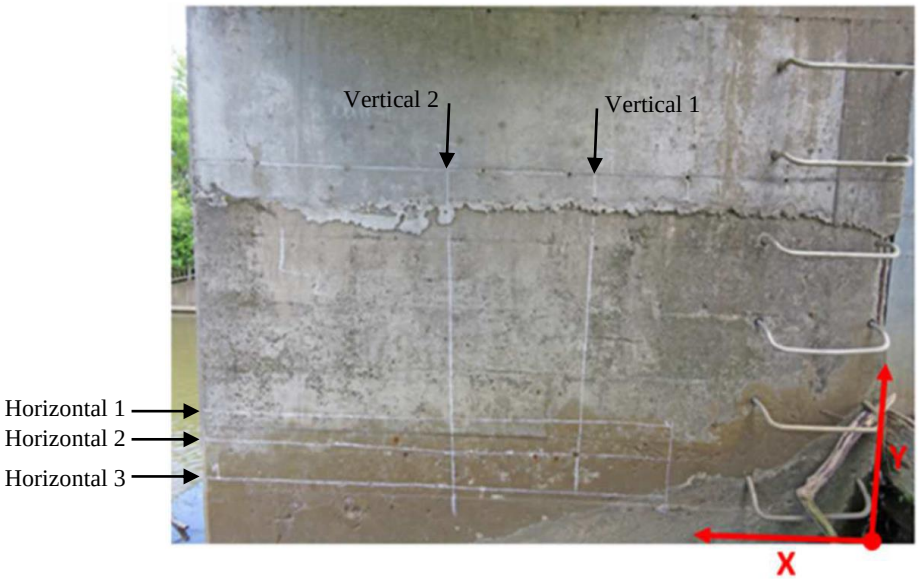

Figure 3-18. Pier three - east wall horizontal and vertical scanned paths

Location of all detected defects larger than 4% area loss is detected by the Haar wavelet analysis (Figure 3-19). The amplitude of pulses in the AG resulted signal of Horizontal 1 rebar is the same as the results of the Haar wavelet. However, there is a pulse in 430 mm distance of Horizontal 1 rebar

Haar wavelet signal which is not the same in the AG signal (Figure 3-19 (a)). The pulse amplitude of the Haar wavelet signals is very close to the AG signals for Horizontal 2 and Horizontal 3 signals (Figure 3-19 (b) and (c)). The location and the amplitude of AG signal pulses are accurately predicted with the Haar wavelet method (Figure 3-19 (d) and (e)).

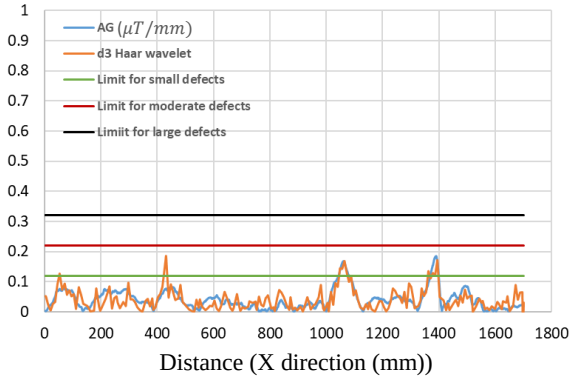

(a)

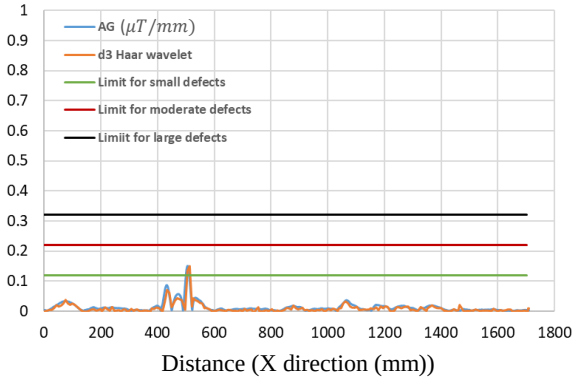

(b)

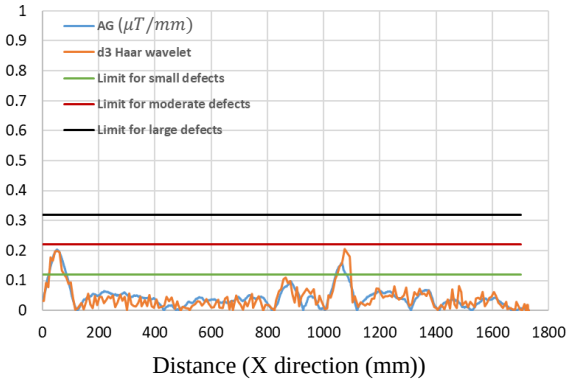

(c)

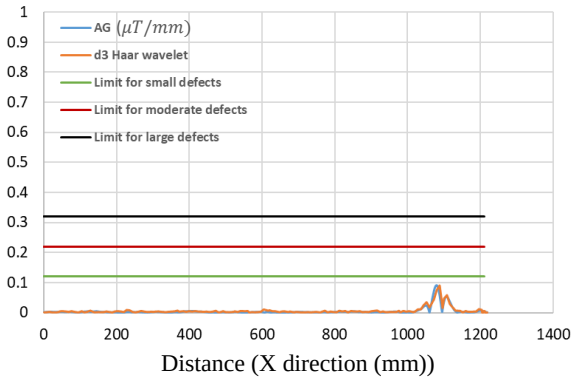

(d)

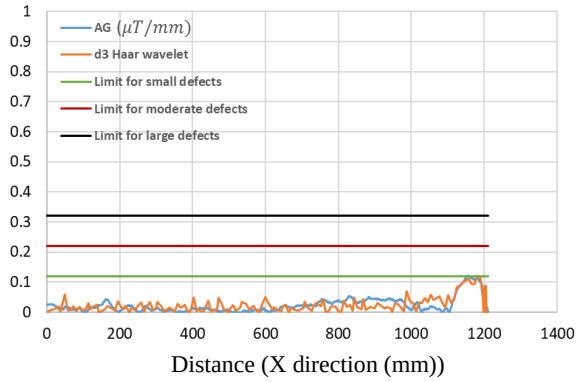

(e)

Figure 3-19. Pier three - east wall AG method and Haar wavelet analysis results. (a) Horizontal 1. (b) Horizontal 2. (c) Horizontal 3. (d) Vertical 1. (e) Vertical 2

The correlation coefficients between the AG and the Haar wavelet vary from 0.68 to 0.93 (Table 7). Vertical 1 has no area loss greater than 4% and has lower similarity. On the other hand, although Horizontal 1 correlation coefficient is relatively low, the location and the amplitude of the area loss higher than 4% are predicted accurately using the Harr wavelet method.

Table 7-Correlation coefficient between the AG and the Haar wavelet signals of the pier three east wall

Rebar	Horizontal 1	Horizontal 2	Horizontal 3	Vertical 1	Vertical 2
Correlation coefficient	0.75	0.90	0.87	0.93	0.68

3.4.8 Pier four - west wall

Two vertical and three horizontal rebar paths were selected to be scanned using the PMI scanner device. The raw magnetic data is recorded over given paths and is transformed to the computer for the analysis (Figure 3-20).

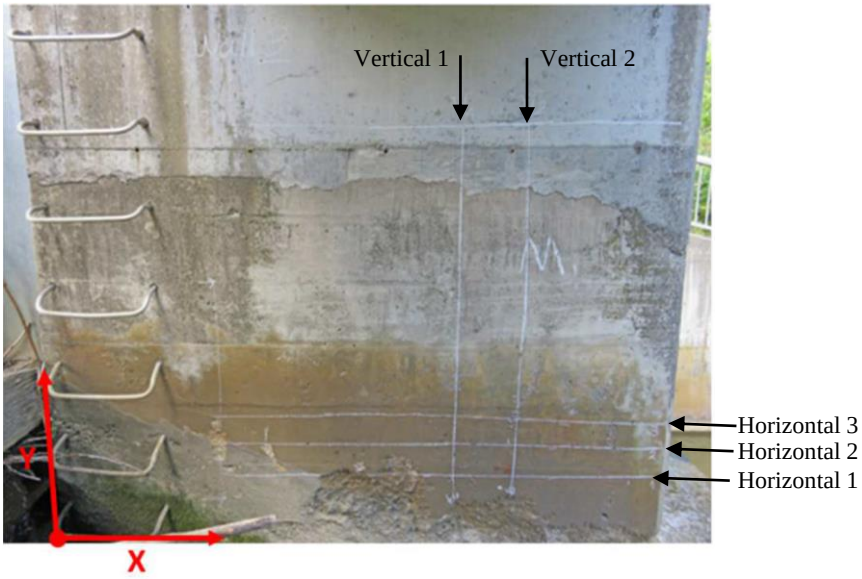

Figure 3-20. Pier four - west wall horizontal and vertical scanned paths

The Haar wavelet analysis predicted all locations with area loss higher than 4% accurately. The amplitude of the area loss is very similar to the AG signal results (Figure 3-21). There is some discrepancy between the results of the Haar wavelet analysis and AG method in Horizontal 3 rebar. However, there is still acceptable similarity between these two signals in the location and the amplitude of corrosion area higher than 4% (Figure 3-21 (c)).

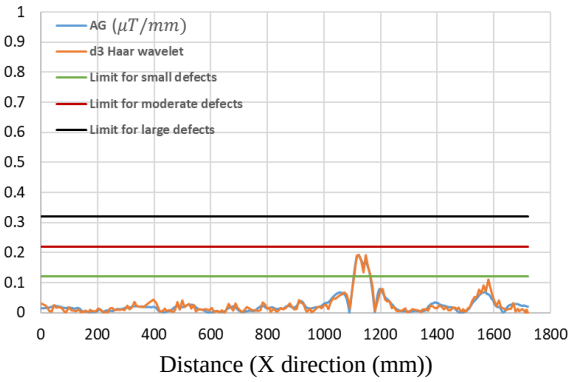

(a)

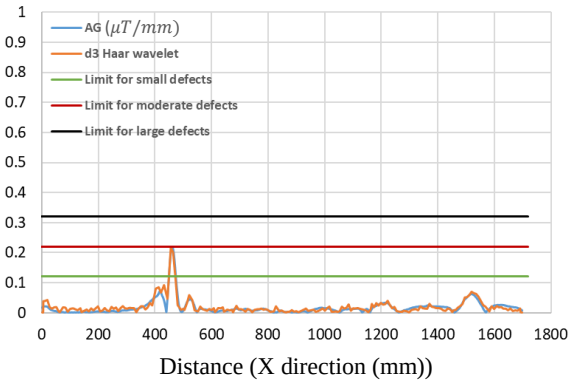

(b)

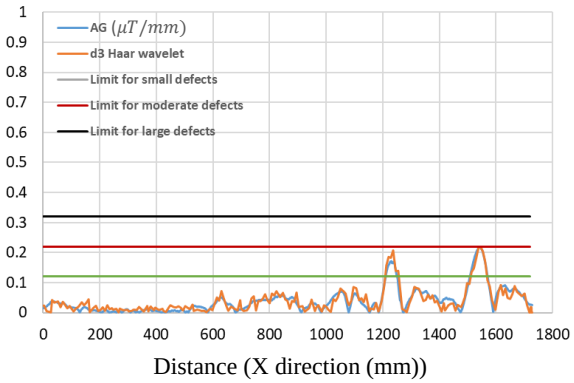

(c)

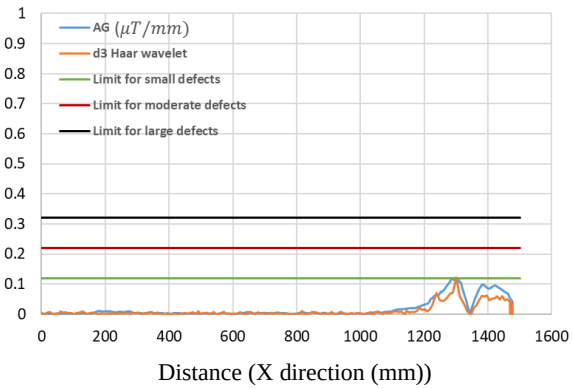

(d)

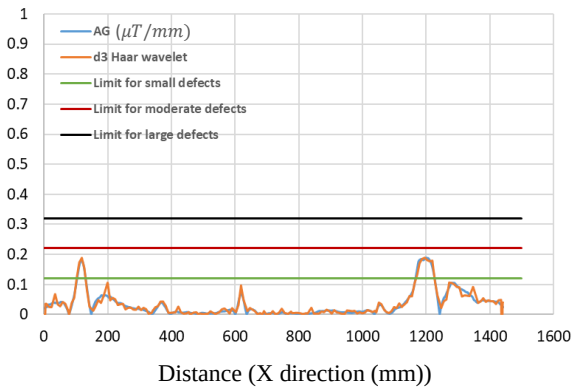

(e)

Figure 3-21. Pier four- west wall AG method and Haar wavelet analysis results. (a) Horizontal 1. (b) Horizontal 2. (c) Horizontal 3. (d) Vertical 1. (e) Vertical 2.

The correlation coefficient analysis values range from 0.94 to 0.98 which demonstrates high similarity between the Haar wavelet and AG signals (Table 8).

Table 8-Correlation coefficient between the AG and the Haar wavelet signals of the pier four west wall

Rebar	Horizontal 1	Horizontal 2	Horizontal 3	Vertical 1	Vertical 2
Correlation coefficient	0.96	0.94	0.95	0.96	0.98

3.4.9 Pier four - east wall

The five scanned paths and the positive movement direction of the PMI scanner device are shown in Figure 3-22.

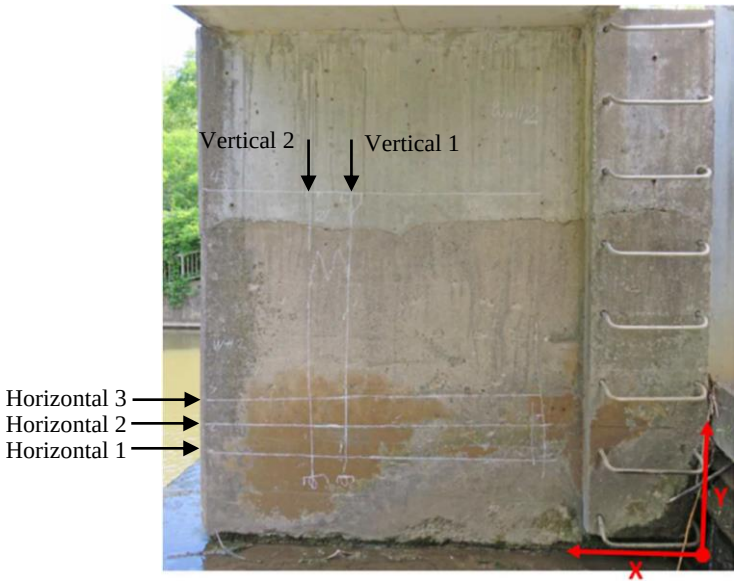

Figure 3-22. Pier four-east wall horizontal and vertical scanned paths

According to the AG method, no rebar has any corrosion loss area greater than 4%, which is the same as the Haar wavelet method results (Figure 3-23). The Horizontal 2 rebar AG result shows two pulses at the 1000mm and 1550mm distances. The location and amplitude of these two pulses are simulated with the Haar wavelet method accurately (Figure 3-23 (b)). This happens exactly for the 450 distance of Vertical 1 rebar.

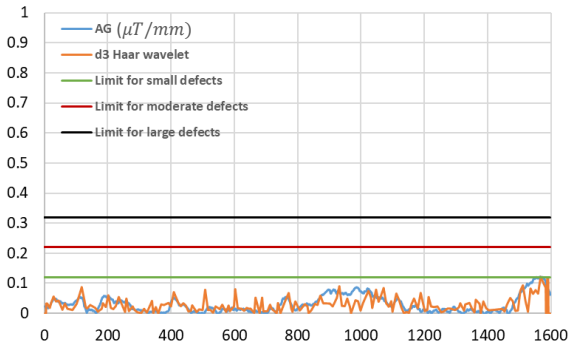

(a)

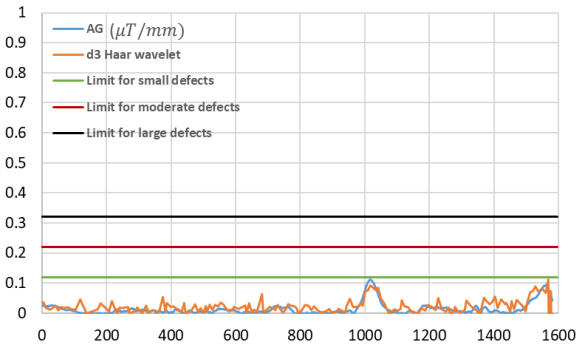

(b)

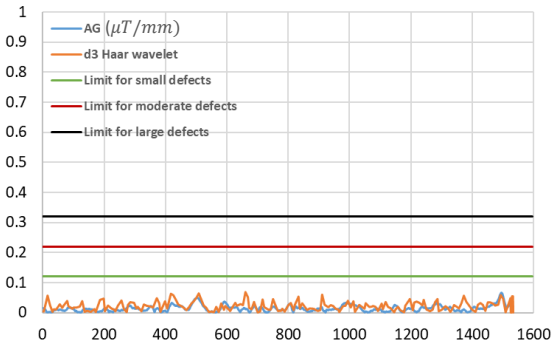

(c)

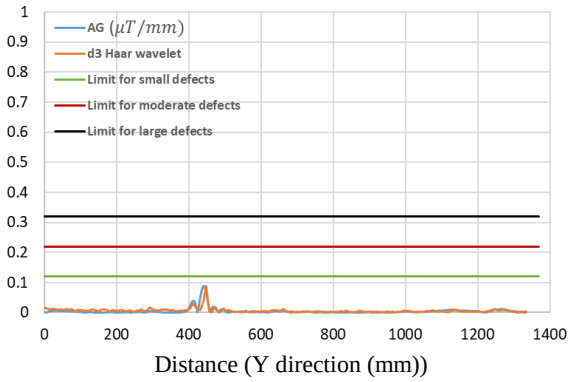

(d)

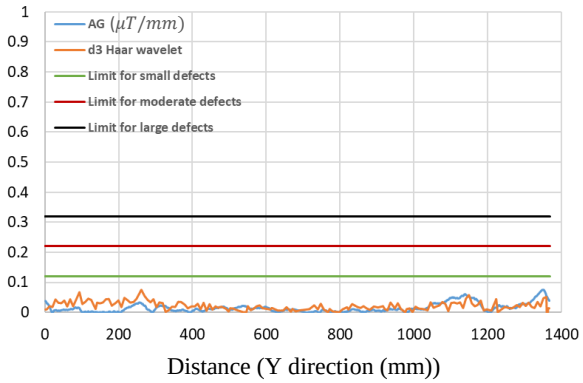

(e)

Figure 3-23. Pier four- east wall AG method and Haar wavelet analysis results. (a) Horizontal 1. (b) Horizontal 2. (c) Horizontal 3. (d) Vertical 1. (e) Vertical 2.

The correlation coefficient values range from 0.26 for Vertical 2 to 0.76 for Vertical 1. Vertical 2 AG method result does not show any specific pulse and there is no area loss greater than 4%. Although the correlation coefficient for Vertical 2 rebar is low, both the AG method and the Haar wavelet method give the same result for the corrosion greater than 4% (Table 9).

Table 9-Correlation coefficient between the AG and the Haar wavelet signals of the pier four east wall

Rebar	Horizontal 1	Horizontal 2	Horizontal 3	Vertical 1	Vertical 2
Correlation coefficient	0.62	0.74	0.37	0.76	0.26

3.4.10 End east wall

Three horizontal and two vertical rebars are scanned using the PMI scanning device. The selected rebars and the positive movement direction of the scanner are shown in Figure 3-24.

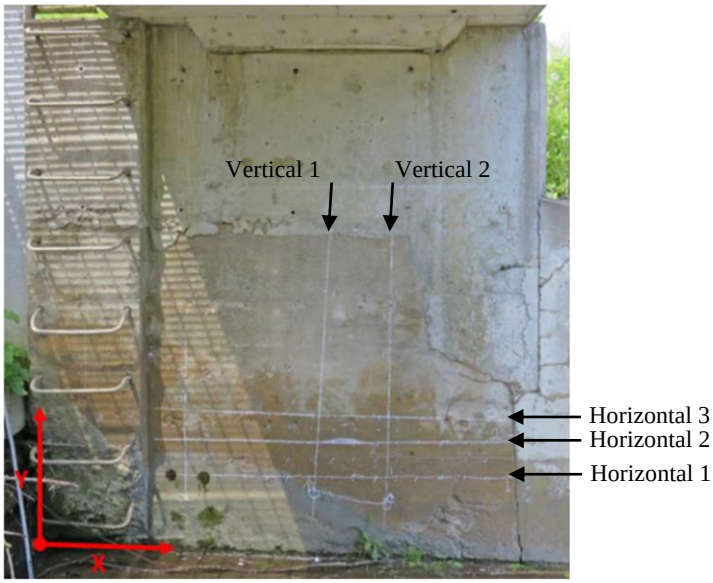

Figure 3-24. End east wall horizontal and vertical scanned paths

According to the AG method all the horizontal rebars have area loss greater than 4%, and the area loss in the vertical rebars is less than 4% (Figure 3-25). The Haar wavelet method detected the location and the value of the area loss in Horizontal 1 rebar (Figure 3-25 (a)). The AG method shows there are five areas with loss greater than 4% in Horizontal 1 rebar, including the 400mm, 680mm, 1200mm, and 1500mm distances, also detected by the Haar wavelet method. However, the Haar wavelet method underestimated the amplitude of the AG signal at the 400mm distance site. The Haar wavelet and AG methods have the same prediction about the location and value of area loss greater than 4% in Horizontal 2 and Horizontal 3 rebars (Figure 3-25 (b) and (c)). While the area loss in Vertical 1 and Vertical 2 rebars are lower than 4%, the AG and the Haar wavelet results are the same about the location and area loss values (Figure 3-25 (d) and (e)).

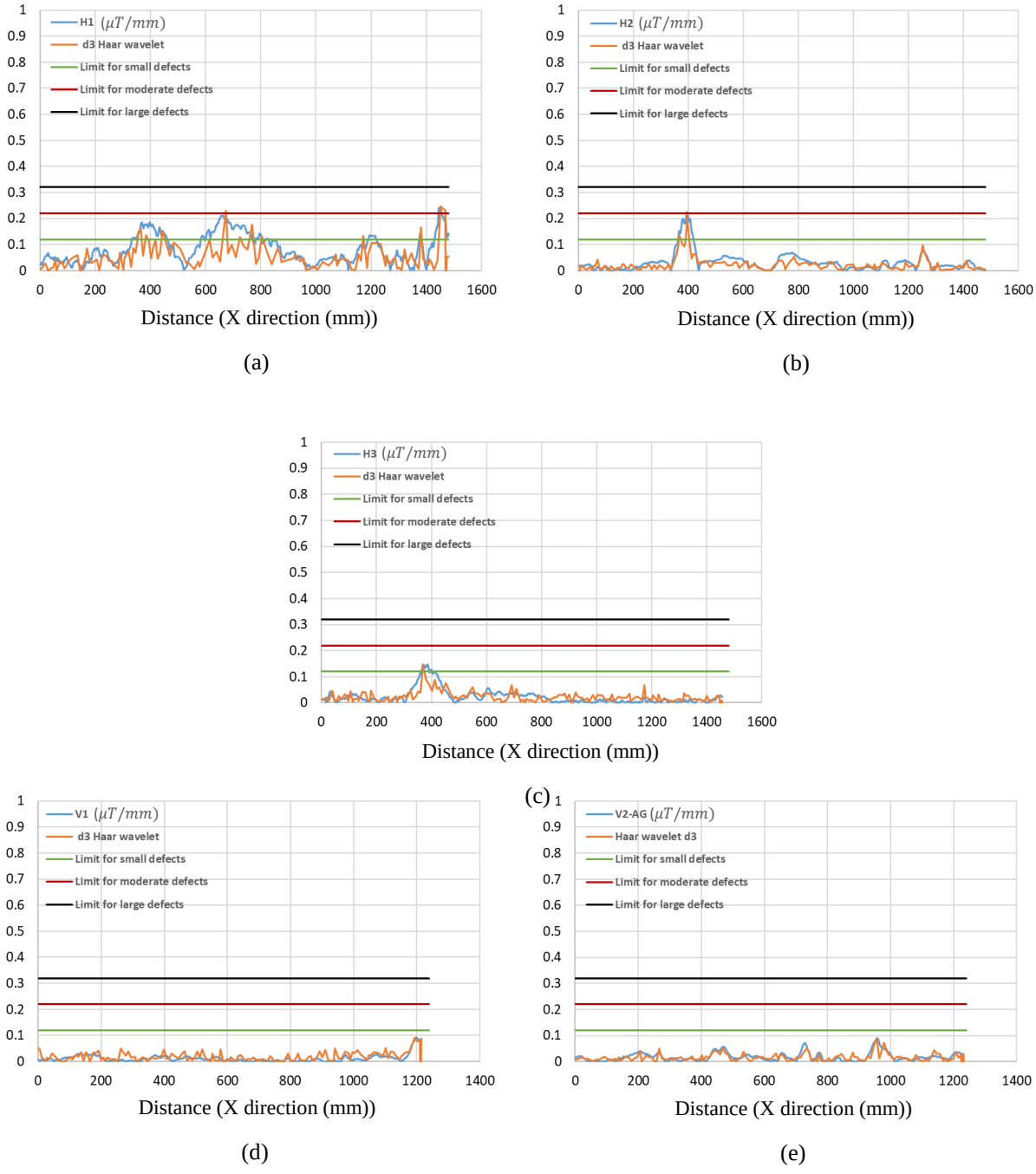

Figure 3-25. End east wall AG method and Haar wavelet analysis results. (a) Horizontal 1. (b) Horizontal 2. (c) Horizontal 3. (d) Vertical 1. (e) Vertical 2.

The similarity between the AG and the Haar wavelet resulted signals is quantified by the correlation coefficient value which varies from 0.69 for Vertical 1 to 0.86 for Horizontal 2 (Table 10). Vertical 1 does not show any area loss greater than 4% and there is some discrepancy between the AG and the Haar wavelet method results specifically before the pulse at 1200mm distance which decreased the correlation coefficient. The single pulse of corrosion in Horizontal 2 is simulated with the same amplitude by AG and the Haar wavelet methods which increased the correlation coefficient between the resulted signals.

Table 10-Correlation coefficient between the AG and the Haar wavelet signals of the pier end east wall

Rebar	Horizontal 1	Horizontal 2	Horizontal 3	Vertical 1	Vertical 2
Correlation coefficient	0.69	0.86	0.70	0.62	0.70

3.4.11 Comparison between AG and Haar wavelet results

A summary of the correlation coefficients of all ten walls is presented in Table 11. The total average value of all correlation coefficients is 0.8. There is also no specific difference between the correlation coefficients of the horizontal and the vertical rebars. The number of detected areas with area loss greater than 4% in Table 12 demonstrates that the AG and the Haar wavelet method detected the same number of areas with greater than 4% area loss. Moreover, pier four east wall has the lower correlation coefficient mean value and the lower number of points with area loss greater than 4%, as expected, given the background noise in the signal. On the other hand, pier two west wall has the highest correlation coefficient mean value and number of points with area loss greater than 4%.

Table 11-Correlation coefficient between the AG and the Haar wavelet signals of all walls

Rebar	Horizontal1	Horizontal2	Horizontal3	Vertical1	Vertical2	Mean
End west wall	0.94	0.92	0.83	0.90	0.93	0.90
Pier one west wall	0.85	0.88	0.89	0.95	0.91	0.90
Pier one east wall	0.84	0.76	0.75	0.86	0.85	0.81
Pier two west wall	0.98	0.99	0.95	0.97	0.94	0.97
Pier two east wall	0.88	0.77	0.82	0.66	0.90	0.81
Pier three west wall	0.17	0.79	0.40	0.72	0.67	0.55
Pier three east wall	0.75	0.90	0.87	0.93	0.68	0.83
Pier four west wall	0.96	0.94	0.95	0.96	0.98	0.96
Pier four east wall	0.62	0.74	0.37	0.76	0.26	0.55
Pier end east wall	0.69	0.86	0.70	0.62	0.70	0.71
Mean	0.77	0.86	0.75	0.83	0.78	0.80

Table 12- Number of the detected area loss greater than 4%

Rebar	AG	Haar wavelet
End west wall	5	4
Pier one west wall	7	6
Pier one east wall	3	4
Pier two west wall	17	17
Pier two east wall	4	4
Pier three west wall	4	3
Pier three east wall	5	6
Pier four west wall	6	6
Pier four east wall	0	0
Pier end east wall	6	6

PART TWO

Simulation of Passive Magnetic Inspection Method (PMI) Signals of Rail Tracks Using the Asymmetric Gaussian Chirplet Model (AGCM)

Chapter 4

LITERATURE REVIEW

The advent of high-speed trains is making railway infrastructure safety, especially rail track integrity, increasingly important. Rail assessment, which is part of railway infrastructure inspection, helps prevent railway traffic accidents, and many researchers have explored different methods to assess rail condition reliably and quickly. Here, a brief review of some significant contributions is presented.

Shi *et al.* (2021) used 3D dynamic stress analysis to assess the geometric irregularity adjacent to the weld toe at welded rail joints, a region prone to fatigue cracking because of the stress concentrations.

Steel rails subject to the growth of multiple fatigue cracks was evaluated by Masoudi Nejad *et al.* (2021) using Acoustic Emissions (AE), which requires overcoming the masking effect of the noise generated by the rolling wheel-rail contacts. This interference impairs the reliability of AE signal pickup by sensors and degrades their accuracy. Nevertheless, to detect growing cracks with AE

technology, rails must be under actual train loads to generate the necessary strains, which increases the cost of detection (Zhang *et al.*, 2021).

In the AE context, Hao *et al.* (2018) presented an adaptive detection method for rail crack detection that combined multi-resolution analysis with an improved Adaptive Line Enhancer (ALE). To get rid of complex noise at high speed, Zhang *et al.* (2018) developed a new rail defect detection method by multi-level Adaptive Noise Cancelling (ANC) with a variable step size, least-mean-squares (VSS-LMS) algorithm. Zhang *et al.* (2015) presented a rail defect detection method based on AE using wavelet transform to simulate signals from defective and defect-free rails. A new ANC method for rail defect detection was evaluated by Liang *et al.* (2015) to decrease undesirable interference and better distinguish the weak signals from background noise. A Hurst exponent-improved ALE for weak rail crack AE signal detection at high speeds was developed by Hao *et al.* (2021) helping make this technology applicable in high-speed railways.

The other common method of continuously inspecting rail track is line-structured light detection, but it remains problematic because any sensor vibration or noise impairs its accuracy, making it more suitable for laboratory use than actual application Cao *et al.* (2020). Jiang *et al.* (2021) used a non-contact laser ultrasonic method to detect rail surface rolling contact fatigue cracks and stated that the detection accuracy of this method is 95%. Teidj (2020) introduced a railhead defect indicator using laser radiation and showed good correlation with other defect detection methods. Pathak *et al.* (2019) worked on rail foot flaw detection based on laser-induced waves.

Chirplet atoms are now widely used in various applications for signal analysis; several examples are listed here. Peng *et al.* (2011) evaluated vibration signals for fault diagnosis in gearboxes using the chirplet transform. Miaofen *et al.* (2021) used a Component Matching Chirplet Transform

(CMCT) to detect faults in wind turbine planetary gearboxes. Spanos *et al.* (2007) worked on processing seismic signals using chirplet decomposition combined with the Wigner-Ville transform. The response of linear systems under earthquake loading was assessed statistically using chirplet transforms by Alderucci *et al.* (2017).

This chapter proposes a new simulation method for rail track magnetic flux density signals extracted by Passive Magnetic Inspection (PMI) technology (Mahbaz *et al.*, 2016), (Mahbaz *et al.*, 2017), (Dusseault *et al.*, 2020), using an Asymmetric Gaussian Chirplet Model (AGCM), based on a combination of experimental and simulation results. In the experiments, three used rail pieces (the "samples") were selected and scanned using Infrastructure Corrosion Assessment Magnetic Method (iCAMM) technology (Mosharafi *et al.*, 2020), and the magnetic flux density values were recorded over various paths prescribed on each sample. The magnetic values which are recorded over the samples are the base data for simulation. Three components (X, Y, Z) of magnetic flux density were measured at each path of the rail and stored with a time signal, allowing positioning because the operator scanned the rail at a constant speed. Thus, each sensor provides three two-dimensional matrices (graphs) by scanning the samples' (t,X), (t,Y),(t,Z), where t is time, yielding the PMI signal for analysis.

Then, the AGCM was used to simulate the collected PMI signals as a basic signal processing method. AGCM uses chirplet atoms for simulation, and each atom is defined with seven parameters. The number of atoms used depends on the complexity of a signal: the more complex the signal, the greater the number of chirplet atoms. In addition to the seven parameters, certain useful features such as the energy and domain of atoms can be used for any scanned rail. Thereby, AGCM simulation leads to a more useful interpretation of data and collection of relevant (useful) parameters.

The capability of AGCM as a signal processing method in simulating PMI rail track signals is presented and its accuracy is evaluated by calculating the differences between the absolute value of PMI signal and simulation results. This absolute value is statistically analyzed. Next, the absolute values of the differences of the measured and simulated signals is fitted against Normal, Log-Normal, Weibull, and Gumbell probability distributions. The goal is to demonstrate that the AGCM is a strong method that allows statistical evaluation (probability) for quick and more reliable detection of rail defects under dynamic conditions.

The following flowchart (Figure 4-1) illustrates the study sequence, explained in more detail in the next sections.

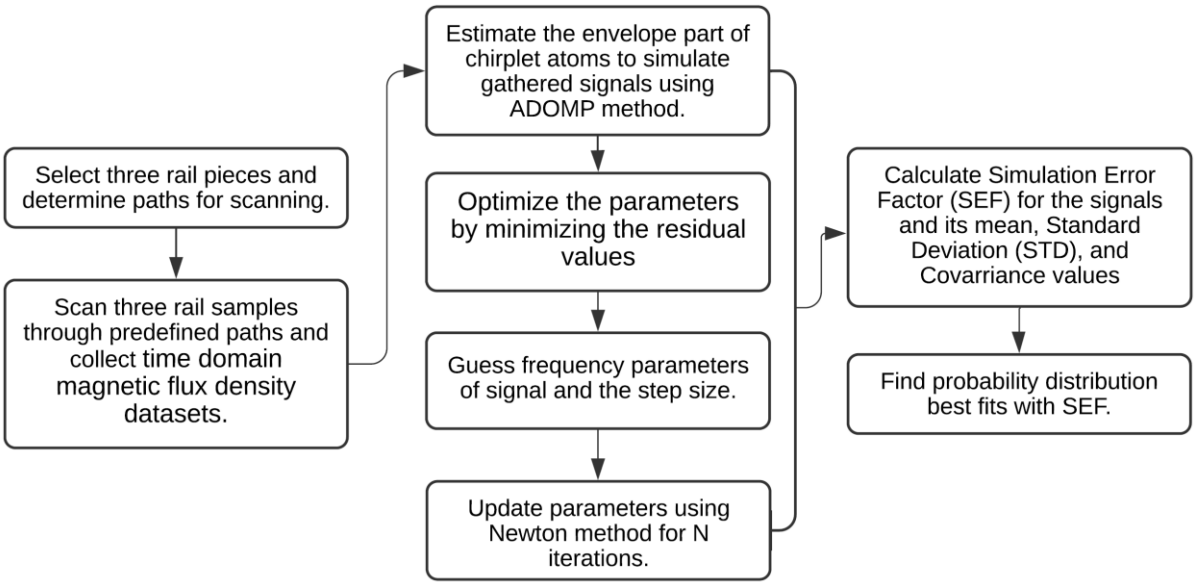

Figure 4-1 Methodology flowchart

Chapter 5

THEORETICAL BACKGROUND

5.1 Rail track inspection method

The Infrastructure Corrosion Assessment Magnetic Method (iCAMM) is used to assess rail track condition. iCAMM technology is based on the PMI concept (Mahbaz *et al.*, 2017), (Dusseault *et al.*, 2020), and it can assess the condition of ferromagnetic materials such as steel rail tracks, and steel reinforcement embedded in concrete and rail tracks. Passive inspection means there is no direct magnetic field imposed nor any extraneous excitation such as an electrical, acoustic, or optical emitter (Ahmad *et al.*, 2015), (Gontarz *et al.*, 2019). Any defects in ferromagnetic specimens lead to changes in the stray energy value (Hubert *et al.*, 1998). Schneider *et al.* (2001) stated that the arrangement of smaller magnetic domains in ferromagnetic materials, which alters the magnetic domain of walls by denser aligned dipoles, is the basis for a change in stray magnetic field energy. In this study the changes in the stray magnetic field energy along the scan lines is used as a reliable method to assess the domain changes that are used to simulate the relation between magnetic flux density and defects on the rail specimens.

5.2 Simulation

The main goal of most signal-simulation methods is to obtain the “best” simulation of real signals in a quantitative manner so that useful information can be extracted. In this research, the sum of chirplet atoms of an Asymmetric Gaussian Chirplet Model (AGCM) is used to simulate signals. This

method can simulate different types of signals such as the pulse-like velocity signals of earthquakes (Sharbati *et al.*, 2020) and the vibration signals from gearboxes during fault diagnosis (Peng *et al.*, 2011). Moreover, the AGCM can lead to methods using genetic algorithms that can lead to higher quality decomposition of multi-component signals (Zanjireh *et al.*, 2013).

This method, introduced by Demirli *et al.* (2014), uses the inner product of real signals with a family of atoms and consists of two operations: the envelope part $E_p(t)$, and the frequency part $F_p(t)$ (Eq.5-1). The two occur simultaneously and each is made up of different parameters: α, β, and τ for the envelope part; f, γ, and θ for the frequency part.

$$A_p(t) = E_p(t)F_p(t) \tag{5-1}$$

$$E_p(t) = exp^{-\alpha\left(1-\beta\ tanh\left(C(t-\tau)\right)\right)(t-\tau)^2} \tag{5-2}$$

$$F_p(t) = \cos(f(t-\tau) + \gamma(t-\tau)^2 + \theta) \tag{5-3}$$

Here, C is a positive constant with a predetermined value. The $\tanh(Ct)$ function equals $-i\tan(iCt)$; it is a hyperbolic function for approximation of a non-continuous function. Its value is 1 when t>0 and -1 when t<0. The $\alpha\ (>0)$ is the bandwidth factor, $\beta \in (-1,1)$ is the asymmetry factor, $\tau\ (>0)$ the time shift factor, $f \in [0,2\pi)$ the center frequency, $\gamma \in [0,2\pi)$ the chirp rate, and $\theta \in [0,2\pi)$ the phase angle (Sharbati *et al.*, 2020).

5.2.1 Simulation of signals using time-frequency atoms

Any signal can be represented using a linear combination of predefined time-frequency atoms. The set of all predefined atoms is the dictionary matrix (D), and the atoms form the columns of the dictionary matrix. The goal of signal decomposition is to extract a subset of M atoms from the D matrix to faithfully represent the signal, subject to accuracy stipulations or other constraints imposed. Any signal can be represented as follows (Bruckstein *et al.*, 2009):

$$y \approx \hat{y} = \sum_{m=1}^{M} a_m d_m \tag{5-4}$$

In this equation d_m represents the mth selected atom from the dictionary matrix columns and a_m is the weighting factor for the mth selected atom. The selected atoms provide a mathematically approximated signal $(\hat{y})$ of the real signal (y). Because of this approximation, there is always an error between the simulated and real signal:

$$error(y, M, D) = \|y - \hat{y}\| = \left\|y - \sum_{m=1}^{M} a_m d_m\right\| \tag{5-5}$$

The error equation depends on the number of atoms, M, and the type of atoms. There are different sets of atoms for simulation, so the simulated signal is not unique. Therefore, a method based on a matching pursuit algorithm (Jabbari *et al.*, 2011; Mallat *et al.*, 1993) and the Newton method is developed to reduce the number of selected atoms and error. The chirplet atoms consist of separate

envelope and frequency parts. The estimation processes for each part are explained in the following sections.

Envelope part

Boßmann and Ma (2015) presented an algorithm to estimate the envelope part and amplitude coefficient a_m of a signal. Assuming that the real signal is $y(t)$ and $G = \{g_m, m = 1,2, \dots, M, M \gg L\}$ is a complete dictionary of AGCM atoms, a signal's envelope part can be expressed as:

$$Env(y)(t) \approx \sum_{m=1}^{L} a_m g_m \tag{5-6}$$

The envelope part is composed of three parameters, $P_E = \{\alpha, \beta, \tau\}$, and the dictionary G includes many envelope atoms, so finding the best sets of AGCM atoms to represent the envelope part of a signal is vital. The Orthogonal Matching Pursuit (OMP) approach alone requires a great deal of computational work. Hence, in the method presented by Boßmann and Ma (2015), called the Adapted Dictionary-free OMP (ADOMP) algorithm, there is no predefined set of atoms and the envelope parameters are calculated by iteratively minimizing the following equation (Eq. 5-7):

$$P_{Ej} = argmin\|R - E_P\|_2 \ \ with \quad Env(y)(t) \approx \sum_{j=1}^{J-1} a_j g_j \tag{5-7}$$

If $\tau = t$, the envelope part $E_P(t)$ will be a maximum. Therefore, we can calculate τ_j and a_j considering the residual R_j as follows:

$$\tau_j = argmax_t \, R_j(t) \tag{5-8}$$

$$a_j = R_j(\tau_j) \tag{5-9}$$

The residual value $R_j(t)$ can be approximated by considering ε as a small positive value and $t \in (\tau_j - \varepsilon, \tau_j + \varepsilon)$ as follows:

$$R_j(t) \approx a_j exp^{-\alpha_j\left(1-\beta_j \tanh\left(C(t-\tau_j)\right)\right)(t-\tau_j)^2} \tag{5-10}$$

The simplified form of this equation is:

$$\log\left(R_j(t)/a_j\right) \approx -\alpha_j \left(1 - \beta_j \tanh\left(C\left(t - \tau_j\right)\right)\right)\left(t - \tau_j\right)^2 \tag{5-11}$$

The two parameters a_j and β_j are calculated by assuming $t_1, t_2, \ldots, t_M$ points around τ_j. Therefore, we can estimate the envelope part of AGCM by finding the envelope parameters α_j, β_j, and τ_j that generate the best matching envelope atoms in each iteration.

Frequency part

In this section the optimization method of the frequency parameters $P_{F_j} = (f_j, \gamma_j, \theta_j)$ is presented. The Newton method is used for this optimization. There are two critical issues in the optimization using Newton's method: the initial guess and the step size. Boßmann and Ma (2015) presented a method to address these issues. After calculation of the envelope part and the AGCM atom g_j after *J* iterations, the residual value equals:

$$R(p_{F1}, p_{F2}, \dots, p_{Fj}) = y - \sum_{j=1}^{J} a_j g_j \tag{5-12}$$

Assume $P = (p_{F1}, p_{F2}, \dots, p_{Fj})$ as a frequency parameters dictionary that can be calculated as follows:

$$P = argmin_p \|R(P)\|_2 \tag{5-13}$$

If we define the R Jacobian matrix at point P $J_R(P)$, after a linear operation for each iteration:

$$R(P') = R(P) + J_R(P)(P' - P) \tag{5-14}$$

Merging these two equations results in:

$$R(P) = -J_R(P)\Delta P \tag{5-15}$$

In this step, by considering h as the step size, the parameter dictionary is updated as follows:

$$P \leftarrow P + h\Delta P \tag{5-16}$$

With this method, the AGCM atoms parameters can be extracted without any need for a predefined AGCM dictionary.

5.3 Probability distributions

Probability distributions can express random variables' properties. Unless there is a strong physical reason to suppose a particular distribution, it is appropriate to explore how different common distributions "fit" the dispersed data. The method used to find the "best fit" distribution was a Probability Paper Plot (PPP) applied to four common probability distributions, Normal, Log-Normal, Gamma and Weibull. In the PPP method, the scale of the graph paper leads to a linear relationship for the plotted data. Then, one may write the Cumulative Distribution Function (CDF) as a linear function and determine the linearity of sample data to find whether the sample data more reliably follows a given distribution. This linearity is determined using the direct regression analysis of the differences between the values proposed by the probability distribution and the real data. The higher the regression value, the better the chosen distribution represents the data. For instance, a random variable follows the Log-Normal distribution if the logarithm of the random variable is normally

distributed. The CDF of the Log-Normal distribution can be written as (Eq.5-17, Eq.5-18, and Eq.5-19):

$$F(x) = P_i = \Phi\left(\frac{\ln(x_i) - \lambda}{\zeta}\right) \tag{5-17}$$

Where:

$$\zeta = \sqrt{\ln\left(1 + \frac{STD^2}{mean^2}\right)} \tag{5-18}$$

$$\lambda = \ln(mean) - \frac{1}{2}\zeta^2 \tag{5-19}$$

Therefore, rearranging for the equation of a line gives (Eq.5-20):

$$\ln(x_i) = \zeta\Phi^{-1}(P_i) + \lambda \tag{5-20}$$

Chapter 6

EXPERIMENTAL SETUP

Three samples were assessed using PMI technology, and magnetic flux density datasets were collected over eight different predetermined paths along each sample's length (Figure 6-1).

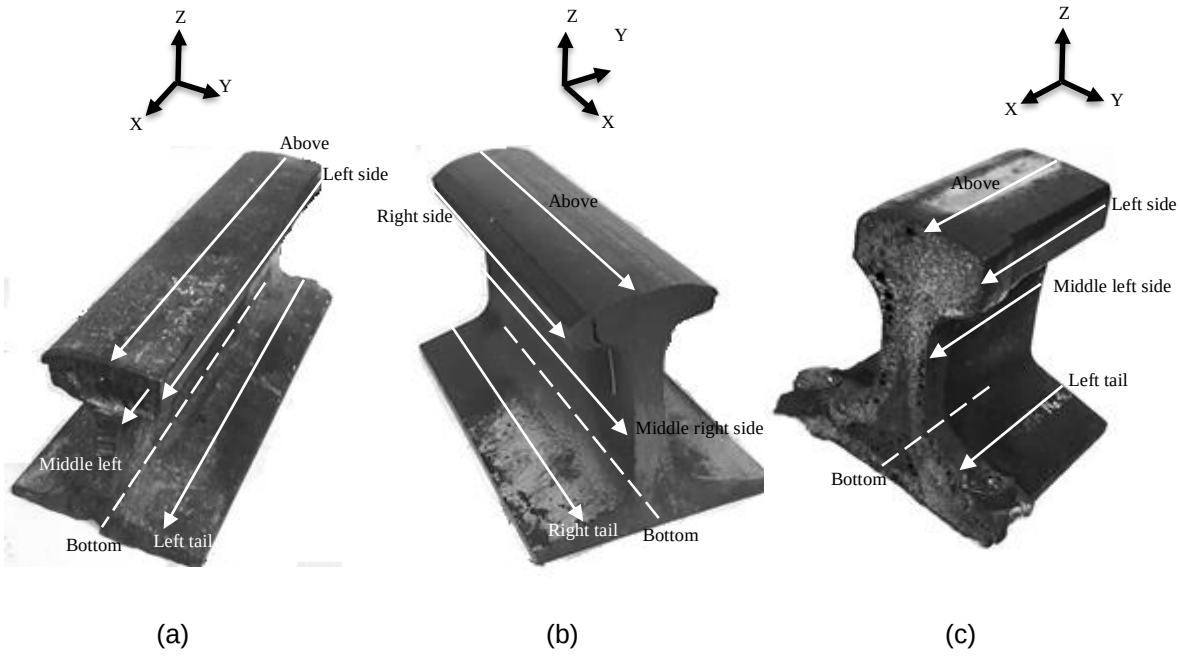

Figure 6-1. The three samples used in the experiments: (a) sample 1; (b) sample 2; (c) sample 3. (White solid lines show the paths marked for scanning).

As shown in Figure 6-2, each sample was placed in a non-ferromagnetic environment, inside an aluminum frame. Next, the operator moved the box, containing the magnetic sensor, along each predetermined path at a constant pace to record three components of magnetic flux density values (in

X, Y, and Z directions). The process was repeated for all chosen paths of the three samples. Since the datasets were recorded at a constant speed, the time of a recording would represent a sensor's location. As an example, Figure 6-3 shows the magnetic flux density versus time of a sensor for "above path-1-X," which refers to the data for sample 1, collected over above path, along X coordinate.

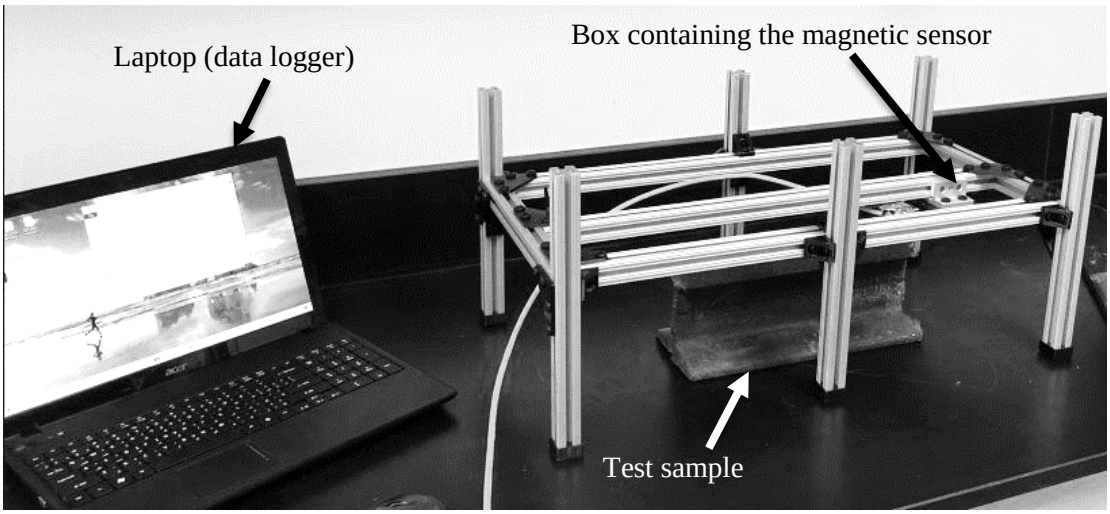

Figure 6-2. Inspection device for experimental measurements of rail track samples

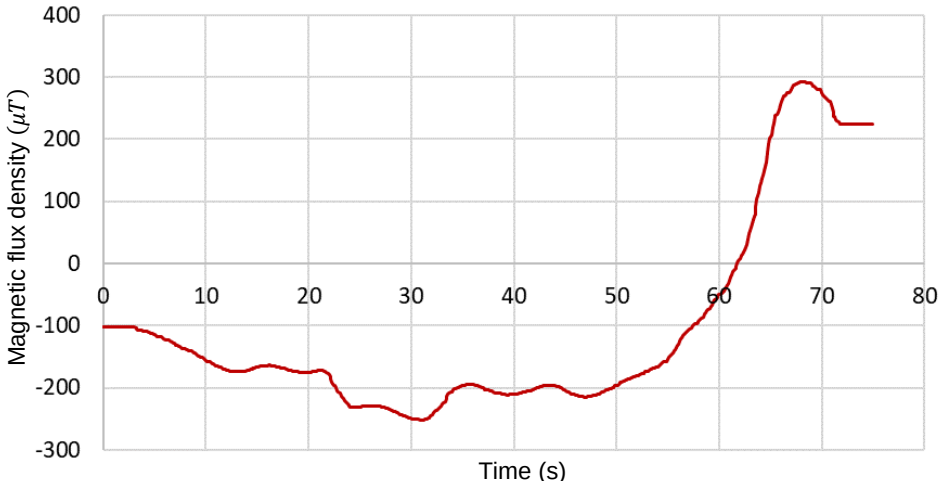

Figure 6-3. Magnetic flux density versus time (Above path-1-X)

Chapter 7

RESULTS

7.1 Accuracy of simulation

PMI results were used as the real signal and simulated with AGCM atoms. Each sensor recorded Magnetic Flux Density (MFD) of the rail samples through specific paths at three coordinates of X, Y, and Z, which were each simulated separately. The real signal here is a two-dimensional graph of time and magnetic flux density. The accuracy of simulation could be defined as the absolute value of difference between real signal and simulated signal. However, because the length and the domain of the magnetic flux density of samples are not the same, the absolute value of the difference is divided by the length of the sample and domain of the MFD. This value is considered as the Simulation Error Factor (SEF) of any signal. Each of the samples has 120 recorded magnetic flux density (consist of 40 three-coordinate data set). Figure **7-1** shows the simulation results and absolute value of difference between real and simulated signal of sample 1, for the datasets recorded over Bottom path. Figure **7-1**(b), Figure **7-1**(e), and Figure **7-1**(h) illustrates the real signal data, and Figure **7-1**(a), Figure **7-1**(d), and Figure **7-1**(g) show the simulated signal. In addition, Figure **7-1**(c), Figure **7-1**(f), and Figure **7-1**(i) represent the absolute error (i.e., difference between real signal and simulated signal along each sample). As seen, the quality of simulation using AGCM atoms is acceptable with no significant difference between the real signal and simulated signal. The SEF of X, Y, and Z signals of sample 1, bottom path, are 0.0160, 0.0066 and 0.0171 respectively. The lowest SEF value belongs to the results

from the Y-axis, and it can also be verified by the comparison of the graph in Figure **7-1**(f) with those in Figure **7-1**(c) and Figure **7-1**(i).

The accuracy of the simulation is different for any sample. Although the SEF is a non-dimensional factor and could not show the accuracy of the simulation solely, the comparison of its values for three samples illustrates which sample was best simulated. Moreover, the comparison of SEF values of X, Y and Z components of samples gains more information about the accuracy of the simulation. All 360 recorded magnetic flux density signals (120 signals of each sample) were simulated using AGCM and the SEF values were calculated. The next part explains the statistical properties of SEF.

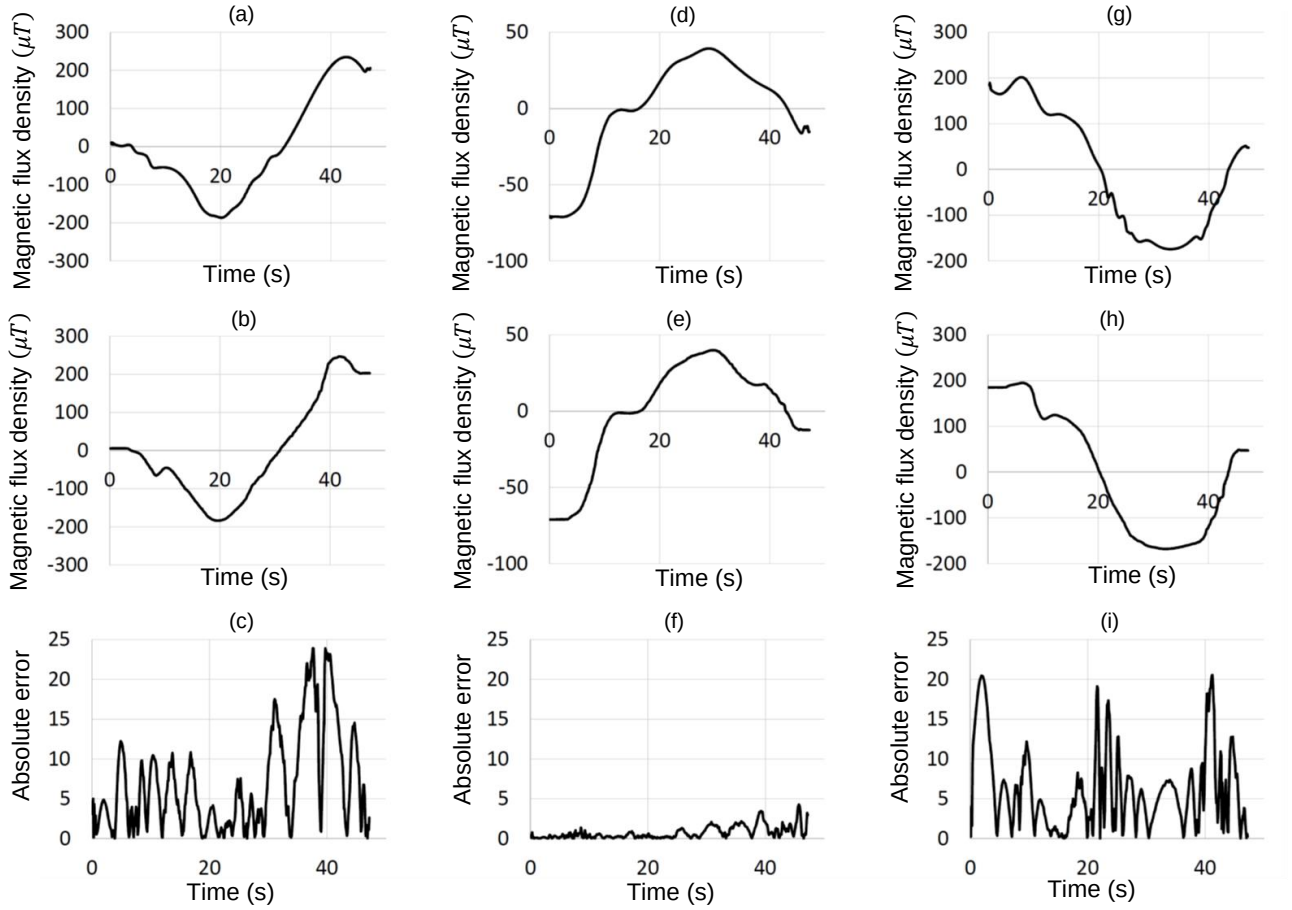

Figure 7-1. Magnetic flux density versus time - Sample 1: (a) Bottom path X- simulated signal; (b) Bottom path X- PMI scanned signal; (c) Bottom path X- absolute error; (d) Bottom path Y- simulated signal; (e) Bottom path Y- PMI scanned signal; (f) Bottom path Y- absolute error; (g) Bottom path Z- simulated signal; (h) Bottom path Z- PMI scanned signal; (i) Bottom path Z- absolute error.

7.2 Statistical properties of SEF

SEF is a random variable and its statistical properties reveal useful information. At first the comparison of the accuracy of simulation of samples could be done by comparison of the mean and standard deviation of SEF values. The lower the mean, the higher the accuracy. Standard deviation shows the dispersion of values. The lower standard deviation shows the values are closer to the mean

value and vice versa. The standard deviation of SEF values is relatively high. This shows that SEF data do not follow a Normal distribution, as in a Normal probability distribution, the data are distributed symmetrically with respect to the mean. Table 1 shows the mean and standard deviation of SEF values. In this table, the Coefficient of Variation (COV) measures the ratio between mean and standard deviation. According to these results, all three samples have approximately the same simulation accuracy (because of the similar mean values). However, according to mean values, the S3 sample has the most accurate simulation results. Considering the X, Y, and Z axis signals simulation, S3X shows the most accurate simulation (Figure 7-2). Figure 7-3 shows sample 3 (S3) represents the lower standard deviation value which means the lower dispersion of SEF values.

Table 13. Statistical properties of SEF.

Signal	Mean	STD	COV
S1	0.024	0.014	0.601
S1X	0.022	0.012	0.573
S1Y	0.026	0.014	0.546
S1Z	0.023	0.015	0.660
S2	0.021	0.013	0.606
S2X	0.021	0.015	0.759
S2Y	0.020	0.008	0.418
S2Z	0.022	0.012	0.566
S3	0.018	0.008	0.453
S3X	0.017	0.008	0.462
S3Y	0.018	0.009	0.485
S3Z	0.020	0.008	0.393

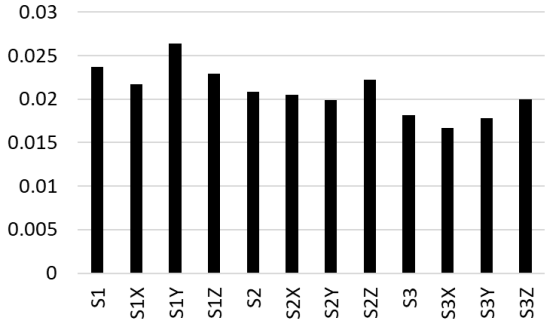

Figure 7-3. Mean of SEF' samples

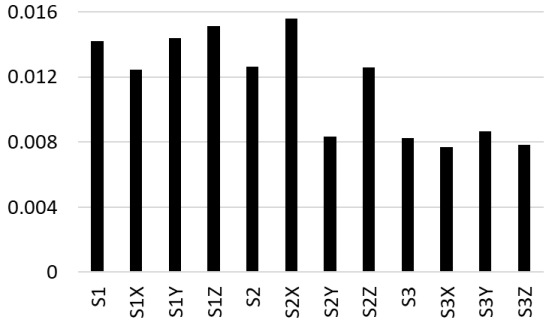

Figure 7-2. STD of SEF' samples

7.3 SEF probability distribution

Finding the distribution that has more compatibility with SEF data has two important advantages: first, finding the outlier data that may be a sign of a problem in the rail track scanning or simulation; and second, evaluating the probability of SEF values for any future simulation at any specific threshold. As stated before, PPP method was used to find the best fit probability distribution and four probability distribution functions (Normal, Log-Normal, Gamma, and Weibull were assessed). Results showed that Log-Normal is the best fit distribution for SEF data (Table 14). Log-Normal paper plot is obtained by plotting the logarithm of the data $\ln(SEF)$ against the Standard Normal Percentage (Figure 7-4).

The Normal distribution, as expected, because of its symmetric function, could not represent the SEF data appropriately and shows lower regression values in comparison with those generated from other probability distributions.

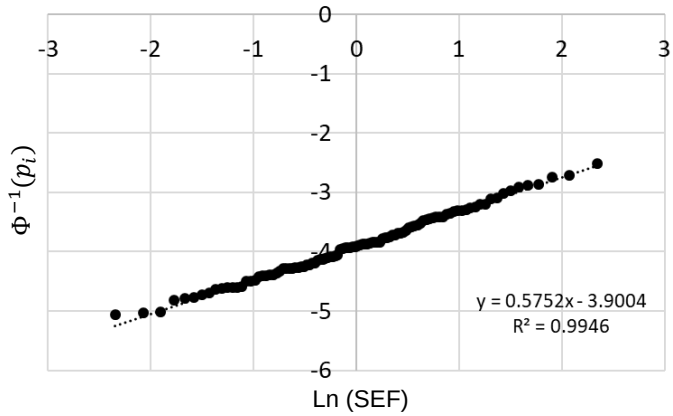

Figure 7-5. PPP method-S1-LogNormal distribution

Table 14. Probability distribution regression

Signal	Regression-Normal Dist.	Regression-LogNormal Dist.	Regression-Weibull Dist.	Regression-Gumbell Dist.
S1	0.867	0.995	0.928	0.973
S1X	0.808	0.976	0.922	0.919
S1Y	0.947	0.980	0.967	0.990
S1Z	0.778	0.979	0.898	0.902
S2	0.890	0.989	0.937	0.974
S2X	0.761	0.969	0.886	0.860
S2Y	0.950	0.965	0.975	0.976
S2Z	0.910	0.969	0.926	0.976
S3	0.908	0.979	0.908	0.971
S3X	0.828	0.924	0.808	0.934
S3Y	0.901	0.990	0.941	0.977
S3Z	0.956	0.986	0.954	0.984
Mean	0.875	0.975	0.921	0.953

Part Three

Conclusions and Future Work

Chapter 8

CONCLUSIONS

The problem of the passive NDT methods is that the magnetic signal is weaker and the background field is higher than active methods. The achievement of passive methods, e.g., PMI, depends on eliminating this background field, which differs from test to test. This research assessed the potential of two methods for simulation the PMI signals of steel rebar and steel rail track effectively.

In the first part of this thesis, the PMI scanner was used to record magnetic flux density versus location of embedded steel reinforcement. Wavelet capability, as a time-frequency function, was assessed to simulate the PMI non-stationary signals, and the Haar wavelet decomposition level 3 of detail was used as the steel reinforcement corrosion indicator, and the AG method was used to verify results. The Haar wavelet detail signals are symmetric with respect to the Y axes. Therefore, for better comparison with the AG signal, the positive part of the Haar wavelet detail signal was considered, and the similarity between the AG and the Haar wavelet signals was assessed visually and using the correlation coefficient.

The Toogood Dam, Markham, Ontario, piers reinforcement was evaluated. Three horizontal and two vertical rebars of each ten given areas included two sides of four piers, and two end embankment walls were scanned using the PMI scanner. The recorded magnetic data was transferred to the computer. Each Haar wavelet signal was scaled with respect to the maximum value of the AG signals, and the following results can be extracted according to this specific case study:

- The number of points identified in the scanned rebar with cross-sectional area loss higher than 4% was almost the same in the AG method and the Haar wavelet method.
- The results of this study shows that the similarity between the AG and the Haar wavelet signals increases with increase of the number of points with area loss higher than 4% (i.e., higher amplitude above the base "noise" level). The pier two west wall rebars have the most points with area loss greater than 4% and also the highest correlation coefficient.
- The Haar wavelet function up-and-down shape correlates with the corrugated surface of the reinforcing rebars and filters other irregularities on the surface of the reinforcement.

The corrugated surface of rebar is different from the smooth surface of rail track. Therefore, in the second part of this research a new method for assessment of rail track condition using magnetic flux density was proposed and the scanned signals were simulated by the Asymmetric Gaussian Chirplet Method (AGCM). Magnetic flux density signal is used as a rail condition indicator. There were three rail samples scanned using PMI technology and magnetic flux density of the samples through several given paths over the length of the samples was recorded. The scanned data was then simulated by AGCM. The accuracy of the simulation was evaluated using the Simulation Error Factor (SEF) which is the absolute value of difference between the scanned signal and the simulated signal divided by length of the rail sample and domain of magnetic flux density of each sample. The results of the simulation for three samples were approximately the same and the best simulation results belonged to

sample 3. The mean of SEF for all recorded data over sample 1, sample 2, and sample 3, were 0.024, 0.021, and 0.018 respectively. Moreover, the standard deviation was 0.014, 0.013, and 0.008 for sample 1, sample 2, and sample 3 respectively, showed the sample 3 SEF values tend more to be close to the mean of SEF values.

Four probability distributions, Normal, Log-Normal, Weibull, and Gumbell, were evaluated using PPP method and regression values for SEF data, and the Log-Normal distribution shows the best compatibility (best regression value) with SEF. Moreover, a Normal distribution showed lower compatibility with SEF values, indicating that symmetric probability distributions cannot represent SEF values properly.

- SEF is a non-dimensional, random variable that can be used to assess quality of rail sample simulation. There is no specific difference between the SEF values of X, Y, and Z magnetic data components.
- Asymmetric probability distributions (Log-Normal) fit better than symmetric probability distributions to SEM values. The Log-Normal distribution regression values are 0.99, 0.99, and 0.98 for S1, S2, and S3 samples respectively.
- PPP graphs (Figure 7-5) help to identify outlier data by finding the points that lie away from the general trend of other points.
- When good quality SEM values are evaluated, expected mean and standard deviation for future assessments' SEM can be predicted.

Chapter 9

CONTRIBUTIONS

Mahbaz *et al*. (2017) modeled actual rebar's geometry in COMSOL and simulated the magnetized defective rebar under a specific value of magnetic field. Then, the magnetic properties of the rebar at a certain distance of the rebar were assessed.

Mosharafi *et al*. (2020) presented a new Fourier-based method for investigation the patterns of magnetic values for different steel rebar defects and categorized the severity of defects according to the PMI magnetic values.

To continue the technical development of PMI, this research presented a wavelet defect detection method in steel rebar. Fourier transform, the conventional method for steel rebar data analysis, decomposes the signal content into a frequency representation. Therefore, the function transforms from the time domain to the frequency domain. The Fourier transform has some limitations. For example, the Fourier transform can specify the frequency content, but because this is not a time-frequency function, it cannot specify when these frequencies occur in time (or where in location). The wavelet transform has a solution to overcome this problem. The time-frequency property of the wavelet transform specifies the time and frequency content at the same time.

Consequently, the newly presented rebar defect detection wavelet method needs less calculating effort to detect the severity and location of defects of steel rebar. Moreover, there are different types of wavelets, like Haar, Bior, Symlet, etc., each with different properties, that can simulate different ferromagnetic materials and surfaces magnetic signals. For instance, in this research the Haar wavelet showed considerable capability in steel rebar defect detection. Nonetheless, it has not been proven to be the optimal approach.

Furthermore, as a new investigation subject, the simulation of rail track PMI signals using the Asymmetric Gaussian Chirplet Model (AGCM) is studied. In general, PMI technology is used for steel rebar defect detection, but this research assessed a signal processing method to simulate the rail track PMI signals. Although both the steel rebar and rail track are made up of steel, they have different surface shapes and different PMI signals as well. The Haar wavelet and Fourier wavy shape tended to correlate with the corrugated surface of the steel rebar. However, the rail has a smooth surface and needs another simulation method.

Chapter 10

FUTURE WORK

In this thesis, innovative methods for the analysis and interpretation of PMI technology magnetic signals were presented. The Haar wavelet decomposition was used for the analysis of magnetic signals, and its ability to detect defect points in steel rebars was demonstrated. Wavelet transform is a well-known method for decomposing signals, and MATLAB™ software has some useful wavelet tools for statistical assessment of decomposing wavelet signals. Moreover, wavelet decomposition approaches use different wavelet types like Haar, Symlet, Bior etc., each with different properties. The capability of other wavelet decompositions to detect defects in other ferromagnetic materials can be assessed in the future. Wavelet function analysis can produce detailed signal representation up to a desired resolution level. Selecting the appropriate step (level) of decomposition depends on the type of wavelet and the detailed signal application. Although in this thesis decomposition level three of the wavelet approximation was used to detect rebar defects, other wavelets and analysis could show desired details at other levels of decomposition (level 4, 5, …).

The calibration of PMI signals affects the rebar assessment results significantly and there is a broad field of research on the PMI calibration methods.

The AGCM capability in the simulation of PMI signals of rail tracks was evaluated in another part of this thesis. AGCM chirplet atoms are constructed of envelope and frequency parts. Each of these

parts includes some specific parameters that have a given value for any simulated signals. These parameters build a data set to extract features for the simulation of particular types of defects in the rail tracks.

Specific defect patterns on rail tracks and their effect on the PMI rail track signals can be studied in future research.

REFERENCES

Abdulkareem, M., Bakhary, N., Vafaei, M., MdNoor, N., NoorMohamed, R. (2019). Application of two-dimensional wavelet transform to detect damage in steel plate structures. Measurement Volume 146, Pages 912-923.

Agarwal, S., Kachroo, P., Regentova, E. (2016). A hybrid model using logistic regression and wavelet transformation to detect traffic incidents. IATSS Research Volume 40, Issue 1, Pages 56-63.

Aharoni, A. (2000). Introduction to the Theory of Ferromagnetism. Oxford: Oxford University Press.

Ahmad, M.I.M., Arifin, A., Abdullah, S., Jusoh, W.Z.W., Singh, S.S.K. (2015). Fatigue crack effect on magnetic flux leakage for A283 grade C steel. Steel and Composite Structures, Vol. 19, No. 6, 2015, 1549-1560.

Alderucci, T., Giunta, F., Muscolino, G. (2017). Evolutionary frequency response function of linear systems subjected to earthquake accelerograms using the adaptive chirplet decomposition. Procedia Engineering, Volume 199, 2017, Pages 1080-1085.

Anuragi, A., Sisodia, D. (2020). Empirical wavelet transform based automated alcoholism detecting using EEG signal features. Biomedical Signal Processing and Control Volume 57, 101777.

ASM Handbooks Online, Volume 17, Nondestructive Evaluation and Quality Control Magnetic Particle Inspection.

Bhavsar, P., Sharma, B., Moscoso-Kingsley, W., Madhavan, V. (2020). Detecting first layer bond quality during FDM 3D printing using a discrete wavelet energy approach. Procedia Manufacturing Volume 48, Pages 718-724.

Blitz, J. (1997). Electrical and Magnetic Methods of Non-Destructive Testing, Chapman and Hall edition, ISBN: 0412791501.

Boßmann, F., Ma, J. (2015). Asymmetric chirplet transform — Part 2: Phase, frequency, and chirp rate. Geophysics, VOL. 81, NO. 6.

Boßmann, F., Ma, J. (2015). Asymmetric chirplet transform for sparse representation of seismic data. Geophysics 2015;80(6): Wd89–100.

Brown, W.F. (1962). Magnetostatic Principles in Ferromagnetism. Amsterdam: Northholland Pub. Co.

Bruckstein, A., Donoho, D., Elad, M. (2009). From sparse solutions of systems of equations to sparse modeling of signals and images. SIAM Rev 2009; 51:34–81.

Burrus, C. S., R. A. Gopinath, and H. Guo (1998). Introduction to Wavelets and Wavelet Transforms (First ed.). Upper Saddle River, New Jersey: Prentice Hall, Inc.

Burrus, C. S., R. A. Gopinath, and H. Guo (1998). Introduction to Wavelets and Wavelet Transforms (First ed.). Upper Saddle River, New Jersey: Prentice Hall, Inc.

C.M.Schneider, O. de Haas, U. Muschiol, N.Cramer, A.Oelsner, M.Klais, O.Schmidt, G.H.Fecher, W.Jark, G.Schönhense. (2001). Photoemission microscopy from magnetically coupled thin-film systems. Journal of Magnetism and Magnetic Materials Volume 233, Issues 1–2, July 2001, Pages 14-20.

Cao, X., Xie, W. (2020). Defect detection method for rail surface based on line-structured light Measurement 159 (2020) 107771.

Demirli, R., Saniie, J. (2014). Asymmetric Gaussian chirplet model and parameter estimation for generalized echo representation. J Franklin Inst. 2014;351(2):907–21.

Döring, W. (1966). Mikromagnetismus. In S. Flügge (Ed.), Handbuch der physic, Springer, Berlin, Heidelberg, New York, Vol. 18/2 ed., pp. 341-437.

Doubov, A.A. (1998). Screening of weld quality using the metal magnetic memory. Weld World, 41, 196-199.

Doubov, A.A. (2000). The express-technique of welded joints examination with use of metal magnetic memory. NDT and E International, 33(6), 351-362.

Dusseault, M. B., Mahbaz, S. B. (2020). System and method for detecting irregularities in rebar in reinforced concrete. United States Patent. Patent No: US 10,533,970 B2.

Elefante, A., Nilsen, M., Sikström, F., Christiansson, A. k, Maggipinto, T., Ancona, A. (2019). Detecting beam offsets in laser welding of closed-square-butt joints by wavelet analysis of an optical process signal. Optics & Laser Technology Volume 109, Pages 178-185.

Feng, B., Lopes, A., Helena, R., Ramos, G. (2018). A new method to detect delamination in composites using chirp-excited Lamb wave and wavelet analysis. NDT & E International Volume 100, Pages 64-73.

Fernandes, B., Titus, M., Karl Nims, D., Ghorbanpoor, A., and Devabhaktuni, V. (2012). “Field Test of Magnetic Methods for Corrosion Detection in Prestressing Strands in Adjacent Box-Beam Bridges. ‘J. Bridge Eng. 17, Special Issue: Nondestructive Evaluation and Testing for Bridge Inspection and Evaluation, 984-988.

Fugal, D. L. (2009). Conceptual wavelets in digital signal processing: an in-depth, practical approach for the non-mathematician (First ed.). Space & Signals Technical Pub.

Gaydecki, P., Fernandes, B., Quek, S., Benitez, D., Miller, G., & Zaid, M. (2007). Inductive and magnetic field inspection systems for bar visualization and corrosion estimation in reinforced and pre-stressed concrete, Nondestructive Testing and Evaluation, 22:4, 255-298.

Gontarz, S., Mączak, J., Szulim, P. (2019). Online Monitoring of Steel Constructions Using Passive Methods. Lecture Notes in Mechanical Engineering, 19: 625-635.

Gontarz, S., Radkowski, S. (2012). Impact of Various Factors on Relationships between Stress and Eigen Magnetic Field in a Steel Specimen, Magnetics, IEEE Transactions on, vol.48, no.3, pp.1143-1154.

Gontarz, S., Radkowski, S., Jinsheng D. (2009). Use of passive magnetic method for stress assessment, Reliability, Maintainability and Safety. ICRMS. 8th International Conference on, vol., no., pp.966-971.

Hao, Q., Shen, Y., Wang, Y., Liu, J. (2021). An adaptive extraction method for rail crack acoustic emission signal under strong wheel-rail rolling noise of high-speed railway. Mechanical Systems and Signal Processing Volume 154, June 2021, 107546.

Hao, Q., Zhang, X., Wang, Y., Shen, Y., Makis, V. (2018). A novel rail defect detection method based on undecimated lifting wavelet packet transform and Shannon entropy-improved adaptive line enhancer. Journal of Sound and Vibration. Volume 425, July 2018, Pages 208-220.

Hubert, A., & Schäfer, R. (1998). Magnetic Domains: The Analysis of Magnetic Microstructures, Springer, Berlin, New York.

Hubert, A., Schafer, R. (1998). Magnetic Domains: The Analysis of Magnetic Microstructures: Springer, Berlin, New York, 696 pp.

Ikram, S., Saleem, S., ZawwarHussain, M. (2021). Approximations to linear Klein–Gordon Equations using Haar wavelet. Ain Shams Engineering Journal. Volume 12, Issue 4, December 2021, Pages 3987-3995.

Jabbari, S., Ghassemian, H. (2011). Modeling of heart systolic murmurs based on multivariate matching pursuit for diagnosis of valvular disorders. Comput Biol Med 2011;41:802–11.

Jiang, Y., Wang, H., Chen, S., Tian, G. (2021). Visual quantitative detection of rail surface crack based on laser ultrasonic technology. Optik, Volume 237, July 2021, 166732.

K.Kerut, E., W.Swan, K., To, F., D.Giles, T., J.Kadowitz, P. (2017). Respiratory sigh associated transient autonomic changes detected with a continuous wavelet method of heart rate variability analysis. Biomedical Signal Processing and Control Volume 38, Pages 143-147.

Kim, K., Choe, D., Kwak, S., Ri, Y., Kim, C. (2021). Haar wavelet method for frequency analysis of the combined functionally graded shells with elastic boundary condition. Thin-Walled Structures, Volume 169, December 2021, 108340.

Kumar, R., Nigam, R., Singh, S. (2022). Selection of suitable mother wavelet along with vanishing moment for the effective detection of crack in a beam. Mechanical Systems and Signal Processing Volume 163, 108136.

Li, B., Zhang, P., Mi, S., Hu, R., Liu, D. (2012). An adaptive morphological gradient lifting wavelet for detecting bearing defects. Mechanical Systems and Signal Processing Volume 29, Pages 415-427.

Li, P., Wang, Q., Zhang, Q., Cao, S., Liu, Y., Zhu, T. (2012). Non-destructive Detection on the Egg Crack Based on Wavelet Transform. IERI Procedia, Volume 2, 2012, Pages 372-382.

Liang, B., Iwnicki, S., Ball, A., Young, A.E. (2015). Adaptive noise cancelling and time–frequency techniques for rail surface defect detection. Mechanical Systems and Signal Processing Volumes 54–55, March 2015, Pages 41-51.

Lilong, T., Qiyuan, Z., Xianxiang, H., Zhili, Z. (2021). Detecting Singularities Based on Wavelet Transform and Eliminating Disturbance from External Environment to the output Signals of Gyroscope. Physics Procedia Volume 25, Pages 853-859.

Liu, X., Ahsan, M., Ahmad, M., Hussian, I., Alqarni, M., Mahmoud, E. (2021). Haar wavelets multi-resolution collocation procedures for two-dimensional nonlinear Schrödinger equation. Alexandria Engineering Journal. Volume 60, Issue 3, June 2021, Pages 3057-3071.

Mahbaz, S.B., (2016). Non-Destructive Passive Magnetic and Ultrasonic Inspection Methods for Condition Assessment of Reinforced Concrete. A thesis presented to University of Waterloo. Waterloo, Ontario, Canada, 2016.

Mahbaz, S.B., Dusseault, M.B., Cascante, G. Vanheeghe, Ph. (2017). Detecting defects in steel reinforcement using the passive magnetic inspection method, J. Environ. Eng. Geoph, 22(2): 153-166.

Mallat, S., Zhang, Z. (1993). Matching pursuits with time-frequency dictionaries. IEEE Trans Signal Process 1993;1993(12):3397–415.

Mancio, M., Zhang, J., Monteiro, P. (2004). Nondestructive surface measurement of corrosion of reinforcing steel in concrete. Canadian Civil Engineer, 21, May 2, pp. 12-14, 18.

Masoudi Nejad, R., Liu, Z., Wenchen, M., Berto, F. (2021). Fatigue reliability assessment of a pearlitic Grade 900A rail steel subjected to multiple cracks. Engineering Failure Analysis. July 2021, 105625.

Miaofen, L., Tianyang, W., Fulei, C., Zhipeng, F. (2021). Component matching chirplet transform via frequency-dependent chirp rate for wind turbine planetary gearbox fault diagnostics under variable speed condition. Mechanical Systems and Signal Processing, Volume 161, December 2021, 107997.

Misiti, M., Y. Misiti, G. Oppenheim, and J.-M. Poggi (1997). Wavelet Toolbox Getting Started Guide (First ed.). Natick, MA: The Mathworks, Inc.

Montgomery. D.C. (2014). Design and analysis of experiments. Eighth edition. John Wiley & sons, Inc.

Morteza, Saadatmorad, Ramazan, AliJafari, Talookolaei, Mohammad, Hadi Pashaei, Samir Khatir. (2021). Damage detection on rectangular laminated composite plates using wavelet based convolutional neural network technique. Composite Structures Volume 278, 114656.

Mosharafi, M., (2020). Improving Passive Magnetic Inspection for Reinforced Concrete Condition Assessment. A thesis presented to University of Waterloo. Waterloo, Ontario, Canada, 2020.

Mosharafi, M., Mahbaz, S.B., Dusseault, M.B. (2020). Statistical methods to assess the reliability of magnetic data recorded over steel corrosion sites, Construction and Building Materials, Volume 264.

Mosharafi, M., Mahbaz, S.B., Dusseault, M.B., Vanheeghe, P (2020). Magnetic detection of corroded steel rebar: Reality and simulations. NDT&E International 110 (2020) 102225.

Ogden, T. (1997). Essential Wavelets for Statistical Applications and Data Analysis (First ed.). Boston: Birkhauser.

Ogden, T. (1997). Essential Wavelets for Statistical Applications and Data Analysis (First ed.). Boston: Birkhauser.

Pathak, M., Alahakoon, S., Spiryagin, M., Cole, C. (2019). Rail foot flaw detection based on a laser induced ultrasonic guided wave method. Measurement Volume 148, December 2019, 106922.

Peng, F., Yu, D., Luo, J. (2011). Sparse signal decomposition method based on multi-scale chirplet and its application to the fault diagnosis of gearboxes. Mechanical Systems and Signal Processing. Volume 25, Issue 2, February 2011, Pages 549-557.

Peng, F., Yu, D., Luo, J. (2011). Sparse signal decomposition method based on multi-scale chirplet and its application to the fault diagnosis of gearboxes. Mech Syst Signal Process 2011;25(2):549–57.

Qian, S. Y. (2001). Assessment of corrosion of reinforcement in concrete. Canadian Civil Engineer, 18(2), 20-21.

Sahoo, S., Kanungo, B., Behera, S., Sabut, S. (2017). Multiresolution wavelet transform based feature extraction and ECG classification to detect cardiac abnormalities. Measurement Volume 108, Pages 55-66

Schneider, C.M., de Haas, O., Muschiol, U., Cramer, N., Oelsner, A., Klais, M., Schmidt, O., Fecher, G.H., Jark, W., Schönhense, G. (2001). Photoemission microscopy from magnetically coupled thin-film systems. Journal of Magnetism and Magnetic Materials Volume 233, Issues 1–2, July 2001, Pages 14-20.

Sharbati, R., Rahimi, R. (2020). Detection and extraction of velocity pulses of near-fault ground motions using asymmetric Gaussian chirplet model. Soil Dynamics and Earthquake Engineering 133 (2020) 106123.

Shi, X., Liu, Y., Liu, Z., Hoh, H. J., Tsang, K. S. (2021). An integrated fatigue assessment approach of rail welds using dynamic 3D FE simulation and strain monitoring technique. Engineering Failure Analysis. Volume 120, February 2021, 105080.

Spanos, P.D., Giaralis, A., Politis, N.P. (2007). Time–frequency representation of earthquake accelerograms and inelastic structural response records using the adaptive chirplet decomposition and empirical mode decomposition. Soil Dynamics and Earthquake Engineering. Volume 27, Issue 7, July 2007, Pages 675-689.

Teidj, S. (2020). Defect Indicators in a Rail Based on Ultrasound Generated by Laser Radiation. Procedia Manufacturing Volume 46, 2020, Pages 863-870.

Wang, Z.D., Gu, Y., Wang, Y.S. (2012). A review of three magnetic NDT technologies. Journal of Magnetism and Magnetic Materials, 324(4): 382-388.

Wilson, J.W., Tian, G.Y., Barrans, S. (2007). Residual magnetic field sensing for stress measurement. Sensors & Actuators: A. Physical, 135(2), 381-387.

Zanjireh, Y., Rezaie, AH., Amindavar, HR. (2013). Multi component signal decomposition based on chirplet pursuit and genetic algorithms. Appl Acoust 2013;74(12): 1333–42.

Zhang, J., Yuan, L., Pu, R., W.Loraamm, R., Yang, G., Wang, J. (2014). Comparison between wavelet spectral features and conventional spectral features in detecting yellow rust for winter wheat. Computers and Electronics in Agriculture Volume 100, Pages 79-87.

Zhang, X., Cui, Y., Wang, Y., Sun, M., Hu, H. (2018). An improved AE detection method of rail defect based on multi-level ANC with VSS-LMS. Mechanical Systems and Signal Processing Volume 99, January 2018, Pages 420-433.

Zhang, X., Feng, N., Wang, Y., Shen, Y. (2015). Acoustic emission detection of rail defect based on wavelet transform and Shannon entropy. Journal of Sound and Vibration Volume 339, March 2015, Pages 419-432.

Zhang, X., Zou Z. (2018). A new rail crack detection method using LSTM network for actual application based on AE technology. Applied Acoustics 142 (2018) 78–86.

Zheng, Z., Washington, S. On selecting an optimal wavelet for detecting singularities in traffic and vehicular data. (2012). Transportation Research Part C: Emerging Technologies Volume 25, Pages 18-33.

Zhou, Y., Gencturk, B., Willam, K., Attar, A. (2015). Carbonation-Induced and Chloride- Induced Corrosion in Reinforced Concrete Structures. Journal of Materials in Civil Engineering, Volume 27 Issue 9.

Appendix A

AGCM MATLAB™ Code

A few MATLAB™ modulus and submodules codes were run to simulate the PMI signals, that should be run together. The code is available upon request if needed.